The Ice Water Paths of Small and Large Ice Species in Hurricanes Arthur (2014) and Irene (2011)

EVAN A. KALINA,[a,b,g] SERGEY Y. MATROSOV,[c,b] JOSEPH J. CIONE,[a,b] FRANK D. MARKS,[a]
JOTHIRAM VIVEKANANDAN,[d] ROBERT A. BLACK,[a] JOHN C. HUBBERT,[d] MICHAEL M. BELL,[e]
DAVID E. KINGSMILL,[c] AND ALLEN B. WHITE[b]

[a] NOAA/Atlantic Oceanographic and Meteorological Laboratory Hurricane Research Division, Miami, Florida
[b] NOAA/Earth System Research Laboratory Physical Sciences Division, Boulder, Colorado
[c] Cooperative Institute for Research in Environmental Sciences, University of Colorado, Boulder, Colorado
[d] Earth Observing Laboratory, National Center for Atmospheric Research,[f] Boulder, Colorado
[e] Department of Atmospheric Science, Colorado State University, Fort Collins, Colorado

(Manuscript received 2 September 2016, in final form 6 January 2017)

ABSTRACT

Dual-polarization scanning radar measurements, air temperature soundings, and a polarimetric radar-based particle identification scheme are used to generate maps and probability density functions (PDFs) of the ice water path (IWP) in Hurricanes Arthur (2014) and Irene (2011) at landfall. The IWP is separated into the contribution from small ice (i.e., ice crystals), termed small-particle IWP, and large ice (i.e., graupel and snow), termed large-particle IWP. Vertically profiling radar data from Hurricane Arthur suggest that the small ice particles detected by the scanning radar have fall velocities mostly greater than $0.25 \, \mathrm{m \, s^{-1}}$ and that the particle identification scheme is capable of distinguishing between small and large ice particles in a mean sense. The IWP maps and PDFs reveal that the total and large-particle IWPs range up to $10 \, \mathrm{kg \, m^{-2}}$, with the largest values confined to intense convective precipitation within the rainbands and eyewall. Small-particle IWP remains mostly $<4 \, \mathrm{kg \, m^{-2}}$, with the largest small-particle IWP values collocated with maxima in the total IWP. PDFs of the small-to-total IWP ratio have shapes that depend on the precipitation type (i.e., intense convective, stratiform, or weak-echo precipitation). The IWP ratio distribution is narrowest (broadest) in intense convective (weak echo) precipitation and peaks at a ratio of about 0.1 (0.3).

1. Introduction

The type, size, and amount of ice particles in a tropical cyclone (TC) are difficult to measure accurately, but the ice characteristics affect the TC structure and evolution through a complex set of interactions with the storm dynamics. Small particles in the form of ice crystals, located aloft within the TC anvil, promote subsident warming below the anvil and cloud-top radiative cooling, thereby altering the atmospheric stability and the horizontal temperature and pressure gradients (Fovell et al. 2009). Ice crystals may also undergo diffusional growth and aggregate into snowflakes, which have a larger fall velocity and can impact the latent heat budget by sublimating (or evaporating, once they melt) as they fall into subsaturated atmospheric layers. In the most intense rainband and eyewall convection, particle vertical velocities are sufficient to support riming of snowflakes into graupel particles, which further affects the latent heat budget when liquid water freezes onto graupel. Observational evidence suggests that the amount of supercooled liquid water available for riming increases with the concentration of African dust in the hurricane environment (Rosenfeld 1999; Andreae et al. 2004; Rosenfeld et al. 2012), an additional complicating influence of TC microphysics. The changes in latent heating posed by the above processes can modify the atmospheric stability, the vertical motion, and ultimately, the TC track and intensity (Lord et al. 1984; McFarquhar et al. 2006; Fovell and Su 2007; Fovell et al. 2009).

Traditionally, ice particle observations above the surface have been obtained via aircraft. Hurricane reconnaissance missions conducted with the NOAA Lockheed WP-3D Orion aircraft have collected several high-quality in situ ice microphysical datasets, including in Hurricanes Ella (1978; Black and Hallett 1986), Allen (1980; Black and Hallett 1986), Irene (1981; Black 1990; Black and Hallett 1986), Norbert (1984; Black 1990), Emily (1987; Black et al. 1994), Claudette (1991; Black and Hallett 1999), and Tina (1992; Black and Hallett 1999). The National Aeronautics and Space Administration DC-8 aircraft has also collected ice microphysics data, such as those from Hurricanes Bonnie (1998; Black et al. 2003) and Humberto (2001; Heymsfield et al. 2006). While the Doppler radars flown on these aircraft can remotely observe frozen precipitation regardless of the aircraft flight level, these radars only measure equivalent radar reflectivity (Z_e) and Doppler velocity, limiting their ability to distinguish between different ice particle types and their sizes and concentrations unless dual frequencies are used. Spaceborne instruments, such as the Cloud Profiling Radar (CPR) on *CloudSat* and the dual-frequency precipitation radar (DPR) on the Global Precipitation Mission Core satellite offer some ability to retrieve bulk ice quantities. However, CPR provides nadir profiles rather than volume scans, while DPR provides a limited number of scans per day of a particular area of interest.

In mid-2013, the upgrade of the U.S. Weather Surveillance Radar-1988 Doppler (WSR-88D; Crum and Alberty 1993) operational network to dual-polarization scanning was completed. The addition of polarimetric information, including the ability to retrieve particle type, size, and amount, represents an opportunity to remotely obtain ice microphysical information in landfalling TCs. However, some questions remain regarding the scope and usefulness of these data. For instance, given the sensitivity limitations of the WSR-88D[1] and the resulting impact on the minimum particle size that can be observed, what are the typical fall velocities of the ice particles detected by the radar? In the context of this limitation, how much of each ice species is present? These questions must be answered quantitatively if we wish to compare such observations with output from model microphysics schemes or to the datasets collected by aircraft and satellites.

In this paper, we present WSR-88D-derived estimates of the relative contributions of ice crystals, snow, and graupel to the total ice water path (IWP) in Hurricanes Arthur (2014) and Irene (2011). We also present vertically pointing S-band radar measurements of the ice particle fall velocities in Hurricane Arthur (2014), allowing us to infer the subset of the ice population observed by the WSR-88D. The results from these two case studies are being used to build an ice microphysics dataset for evaluation of TC numerical simulations, which are sensitive to the chosen model microphysics (e.g., see Fovell et al. 2009, 2016; Islam et al. 2015; Chan and Chan 2016; and references therein). These efforts are of interest to NOAA's Hurricane Forecast Improvement Program (HFIP), which relies on observations to evaluate and improve the operational Hurricane Weather Research and Forecasting Model (HWRF).

2. Background

The interested reader is referred to Balakrishnan and Zrnić (1990), Herzegh and Jameson (1992), Zrnić and Ryzhkov (1999), Bringi and Chandrasekar (2001), and Kumjian and Ryzhkov (2008) for an understanding of the dual-polarization radar differential reflectivity Z_{DR}, differential phase Φ_{DP}, specific differential phase K_{DP}, and the copolar correlation coefficient at zero lag ρ_{HV} that are utilized in this study. Recently, dual-polarization radar has been used extensively to study continental thunderstorms (e.g., Bluestein et al. 2007; Romine et al. 2008; Frame et al. 2009; Snyder et al. 2010; Palmer et al. 2011; Wurman et al. 2012; Kalina et al. 2014; Kumjian and Deierling 2015; Melnikov et al. 2015; Friedrich et al. 2016a,b; Tanamachi and Heinselman 2016; and references therein), but limited research has been conducted in TCs. Van Den Broeke (2013) used polarimetric radar data to analyze the scattering characteristics of birds and insects trapped in the eyes of Hurricanes Irene (2011) and Sandy (2012), but did not examine the data from a meteorological perspective. Griffin et al. (2014) used data from the Norman, Oklahoma (KOUN), polarimetric WSR-88D to examine the reintensification of Tropical Storm Erin (2007) over Oklahoma. However, the microphysical characteristics of this overland system likely differed from those of a landfalling TC.

Observational and modeling studies provide evidence for two polarimetrically distinct types of ice in mixed-phased clouds: 1) ice crystals, which possess large intrinsic Z_{DR} and K_{DP} because of their nonspherical shape and preferential orientation; and 2) snowflake aggregates and graupel that are relatively isotropic, with Z_{DR} and K_{DP} that are closer to zero (Hubbert et al. 2014a,b). In TCs, ice crystals that originate in the eyewall convection are advected into the stratiform region by the secondary circulation, where they drift downward and grow by diffusion. These particles may circulate around the storm as many as 1.5 times as they are transported by the azimuthal wind (Marks and Houze 1987). Most updraft–downdraft couplets colder than $-2°C$

---

[1] For a dual-polarized WSR-88D operating in precipitation mode, an echo of $-18.5\,dBZ_e$ is required to achieve a signal-to-noise ratio of 0 dB at 10-km range (Melnikov et al. 2011).

also contain frozen particles of at least 0.5 mm in diameter that are nearly spherical, which Black and Hallett (1986) identified as graupel in data from airborne particle probes. In contrast, snowflake aggregates predominate in stratiform regions (Black and Hallett 1986). Such aggregates tend to be rapidly advected, both radially and azimuthally, throughout the stratiform regions of the TC (Black and Hallett 1986; Houze et al. 1992).

One of the most powerful applications of polarimetric radar is to use the Z_e, Z_{DR}, K_{DP}, and other measured variables to determine the dominant particle type within the radar volume. Typically, a fuzzy-logic algorithm is used for this purpose (e.g., Vivekanandan et al. 1999; Zrnić et al. 2001; Park et al. 2009; Snyder et al. 2010). For each variable and hydrometeor class, membership functions that range from zero to one describe how likely it is that a certain value of the radar variable is associated with a given hydrometeor class. The values of the membership functions are then accumulated (summed or multiplied) across all radar variables, and the hydrometeor class with the largest total (i.e., interest value) is assigned to the radar gate. This technique was applied to a TC by May et al. (2008) to document the microphysical structure (their Fig. 7) of TC Ingrid (2005) near northern Australia. Near the strongest implied upward vertical velocities, they found evidence for a rain–hail mix below the melting layer, capped by wet graupel that extended up to −20°C in areas with $Z_e > 25\,\mathrm{dB}Z_e$, in rough agreement with in situ aircraft studies conducted by Black and Hallett (1986, 1999), Marks and Houze (1987), and Black et al. (1994, 1996). Above the graupel and in regions of weaker vertical air motion above the melting layer, the hydrometeors mainly consisted of dry, low-density snow (there was no ice crystal class in the scheme).

More recently, polarimetric radar data have been used to infer characteristics of the drop size distribution in TCs and to compare such estimates with those produced by model microphysics schemes (Brown et al. 2016). However, such an analysis has not been conducted for frozen hydrometeors. In this work, we use polarimetric radar data in Hurricanes Arthur and Irene to estimate the IWP and the relative contribution from ice crystals versus snow and graupel to the IWP. This work is intended as the first step toward evaluating the performance of model microphysics schemes above the melting layer in TCs.

3. Instruments, data, and methods

a. Scanning WSR-88D in Morehead City, North Carolina

1) OVERVIEW

Polarimetric radar data were obtained from the WSR-88D site in Morehead City, North Carolina (KMHX) for Hurricanes Arthur (2014; Fig. 1) and Irene (2011; Fig. 2). The WSR-88D operated in volume coverage pattern (VCP) 212, scanning at 14 elevation angles: 0.5°, 0.9°, 1.3°, 1.8°, 2.4°, 3.1°, 4.0°, 5.1°, 6.4°, 8.0°, 10.0°, 12.5°, 15.6°, and 19.5° (OFCM 2016). Both storms made landfall ~27 km to the east-southeast of KMHX (Fig. 3) at 1200 UTC 27 August 2011 (Irene) and 0315 UTC 4 July 2014 (Arthur). Thus, excellent radar coverage was obtained. Irene and Arthur were of similar intensity at landfall, with maximum 1-min average wind speeds of 75 kt (1 kt = 0.51 m s^{-1}; Irene; Avila and Cangialosi 2011) and 85 kt (Arthur; Berg 2015). Irene was under the influence of moderate southwesterly wind shear[2] (9.2 m s^{-1} from 207°), which caused the convection to be displaced primarily to the north of the center until landfall (Fig. 2). In contrast, Arthur experienced light northwesterly wind shear (3.5 m s^{-1} from 303°), which likely contributed to its symmetric precipitation distribution (Fig. 1; Cione et al. 2013). For each hurricane, five radar volume scans were selected, with the 0.5° plan position indicators (PPIs) from these volumes shown in Figs. 1 and 2. These specific volume scans were chosen because 1) they captured the time evolution of the storm during the period of observation by the radar, and 2) at least 50% of the eyewall precipitation was located within 45- to ~145-km range of KMHX, the area over which IWP estimates can be obtained (discussed later; blue range rings in Figs. 1 and 2).

2) K_{DP} CALCULATION AND PARTICLE IDENTIFICATION SCHEME

After the radar volume scans were selected, several steps were taken to process the data, similar to the methods described in Kalina et al. (2016) and Friedrich et al. (2016a). First, the National Center for Atmospheric Research's (NCAR) Radx C++ software package (https://www.ral.ucar.edu/projects/titan/docs/radial_formats/radx.html) was used to calculate K_{DP} from the Φ_{DP} measured by the radar. A finite-impulse response filter with a length of 10 range gates (2.5 km in total) was iteratively applied to Φ_{DP} four times to smooth it. K_{DP} was then calculated from the smoothed Φ_{DP} over nine range gates, centered on the gate of interest.

The NCAR particle identification scheme (PID; Vivekanandan et al. 1999) was then applied to each volume scan. The PID is a fuzzy-logic scheme that uses trapezoidal membership functions to determine the one

---

[2] The shear vector was calculated from Global Forecast System (GFS) operational analyses by removing the TC vortex and taking the vector difference in the 850–200-hPa winds averaged over the area within 500 km of the TC center.
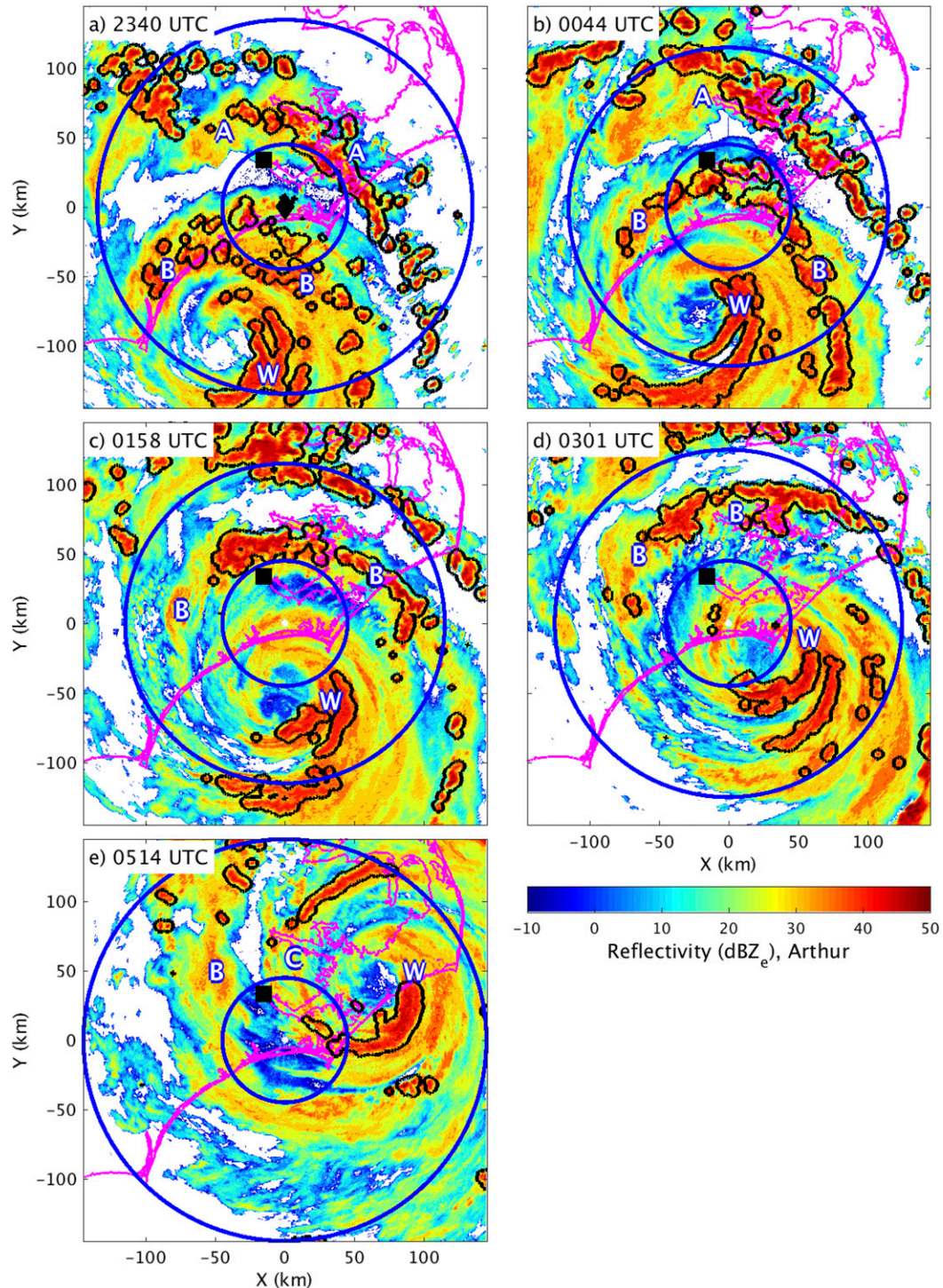
FIG. 1. PPIs at 0.5°-elevation angle of equivalent radar reflectivity in Hurricane Arthur at (a) 2340, (b) 0044, (c) 0158, (d) 0301, and (e) 0514 UTC 3–4 Jul 2014 from the WSR-88D in Morehead City. The black boundaries enclose regions of convective precipitation, as identified by the Steiner et al. (1995) convective–stratiform separation algorithm. The blue range rings indicate the limits of the ice water path calculations shown in Figs. 10–13. The letters A–C denote the approximate radial locations of rainbands discussed in the text. The W indicates the radial location of the eyewall. The black square shows the location of the vertically profiling radar in New Bern. The black diamond in (a) indicates the 0000 UTC 4 Jul 2014 sounding launch location. The coast is outlined in magenta.
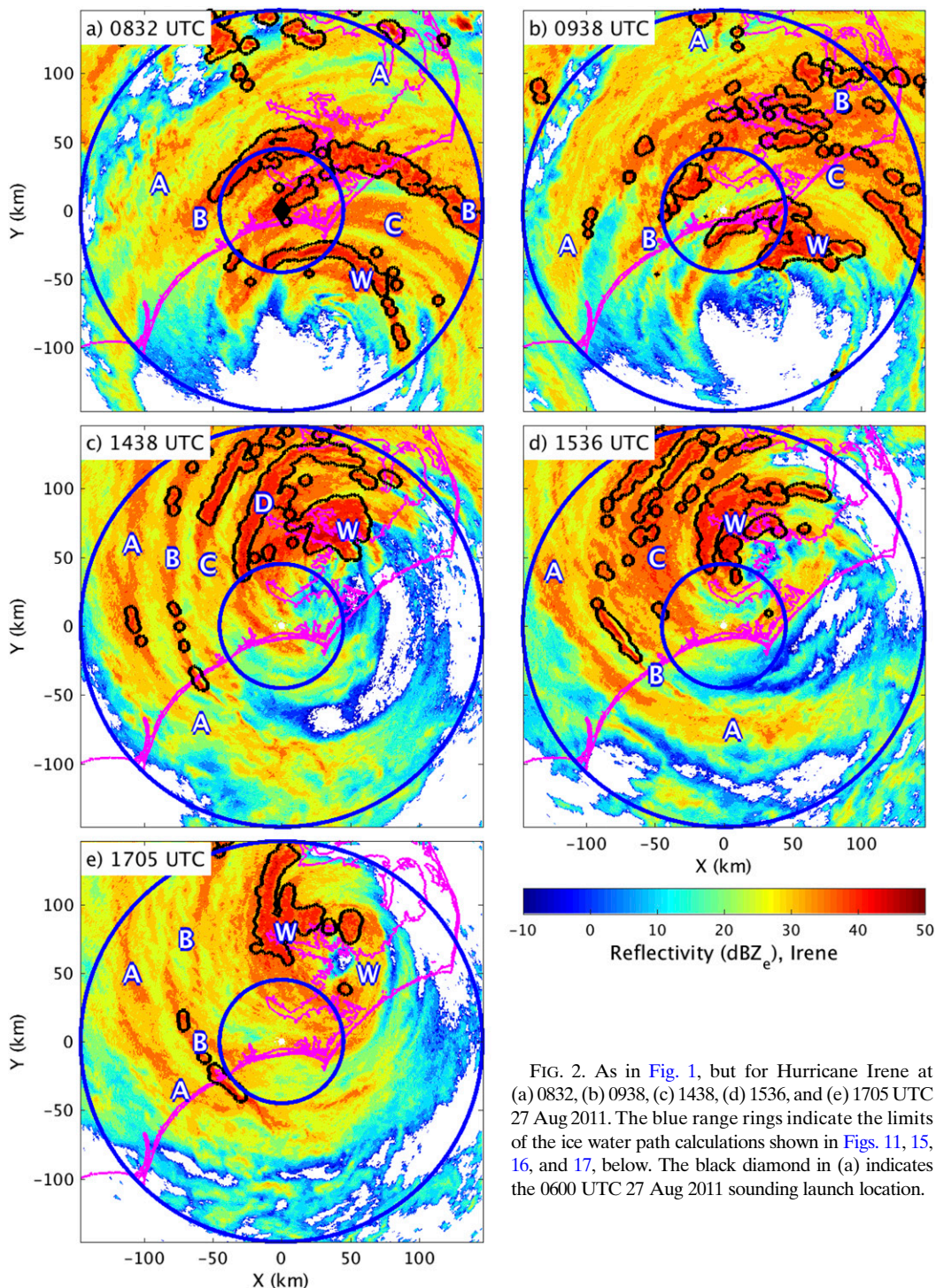
FIG. 2. As in Fig. 1, but for Hurricane Irene at (a) 0832, (b) 0938, (c) 1438, (d) 1536, and (e) 1705 UTC 27 Aug 2011. The blue range rings indicate the limits of the ice water path calculations shown in Figs. 11, 15, 16, and 17, below. The black diamond in (a) indicates the 0600 UTC 27 Aug 2011 sounding launch location.

hydrometeor species that makes the dominant contribution to the radar signal in a given radar range gate. The PID considers seven input variables: Z_e, Z_{DR}, K_{DP}, ρ_{HV}, standard deviations of Z_{DR} and Φ_{DP}, and air temperature; Z_e, Z_{DR}, and ρ_{HV} were smoothed using a

median filter with a length of five range gates (1.25 km in total) to reduce noise. Air temperature profiles were obtained from rawinsonde launches at KMHX at 0600 UTC 27 August 2011 (Irene) and 0000 UTC 4 July 2014 (Arthur). These soundings were launched
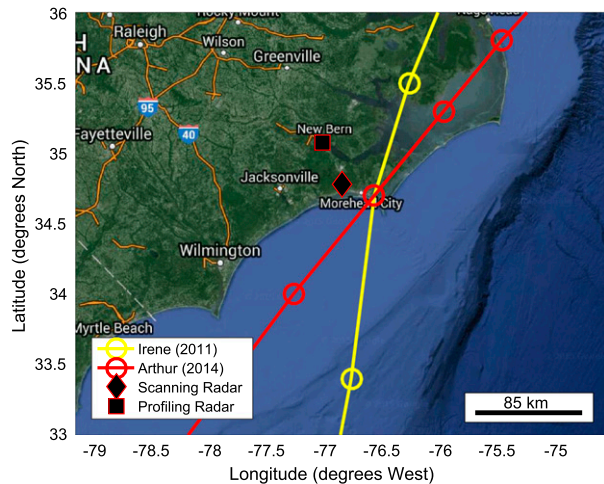
FIG. 3. Tracks of Hurricanes Irene (2011; yellow line) and Arthur (2014; red line). The open circles on the tracks indicate center positions from the hurricane best track. The scanning and profiling radar positions are indicated by the diamond and square, respectively.
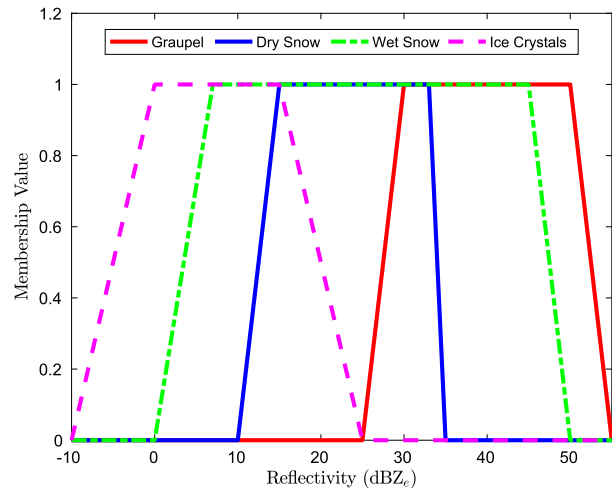

FIG. 4. Trapezoidal membership functions used in the Vivekanandan et al. (1999) particle identification scheme for the equivalent radar reflectivity of graupel (red line), dry snow (blue line), wet snow (green line), and regular/irregular ice crystals (magenta line).

at one-third (Arthur) and one-half (Irene) of the radial distance between the principal rainband and the TC center and were selected in an attempt to minimize the error in the temperature profile between the relatively cooler rainbands and the relatively warmer eyewall. An alternative to this approach would be to use three-dimensional temperature analyses from a mesoscale model as input to the PID to capture the spatial dependence of the temperature profile within the TC.

The five hydrometeor classes from the PID that we consider in this study are ice crystals, irregular ice crystals,[3] dry snow, wet snow, and graupel/small hail. An example of the membership functions for Z_e and each of the aforementioned hydrometeor classes is shown in Fig. 4. Each function ranges in value from 0 to 1, with 1 indicating the range of Z_e that is most typically associated with a given ice species. The membership functions for the remaining variables are two-dimensional trapezoidal functions of Z_e and the variable itself. Figure 5 shows the two-dimensional region over which the values of these membership functions are equal to one for Z_{DR} (Fig. 5a), K_{DP} (Fig. 5b), ρ_{HV} (Fig. 5c), standard deviations of Z_{DR} and Φ_{DP} (Fig. 5d), and air temperature (Fig. 5e) for each hydrometeor class. The membership function values are aggregated in a weighted sum to compute an interest value for each of the hydrometeor classes.

The class with the largest interest value is assigned to the radar gate.

The performance of hydrometeor classification schemes can be degraded by nonuniform beamfilling, which increases with distance from the radar (Ryzhkov 2007; Park et al. 2009; Kumjian 2013). Radar data affected by nonuniform beamfilling exhibit reduced signal-to-noise ratios and increased statistical fluctuations. At 45–145 km from the radar (i.e., the approximate range over which the PID was computed in this study), the KMHX cross-beam resolution varied from 0.73 to 2.4 km. To decrease the likelihood that nonuniform beamfilling and other artifacts negatively impacted the results, the PID was only computed for range gates that had signal-to-noise ratios ≥ 3 dB and interest values (i.e., the weighted sums of the membership function values over each variable) ≥ 0.5 for at least one particle class. Together with the smoothing of the input radar variables, these steps excluded data from the analysis that were characterized by poor signal, poor confidence, and/or noise. However, future studies may wish to apply the method discussed here exclusively at closer ranges to the radar (<100 km) if the effects of large cross-beam resolutions are of particular concern.

3) REGRIDDING STRATEGY

After the PID was applied, the Radx software program was used to regrid the radar data from polar coordinates to 1) a radar volume in Cartesian coordinates in (x, y) with the elevation angles preserved as the vertical coordinate, and 2) a horizontal slice at $h = 2$ km.

---

[3] Irregular ice crystals are those ice crystals that are quasi-spherical and do not have a regular habit (Nousiainen and McFarquhar 2004; Iwabuchi et al. 2012).
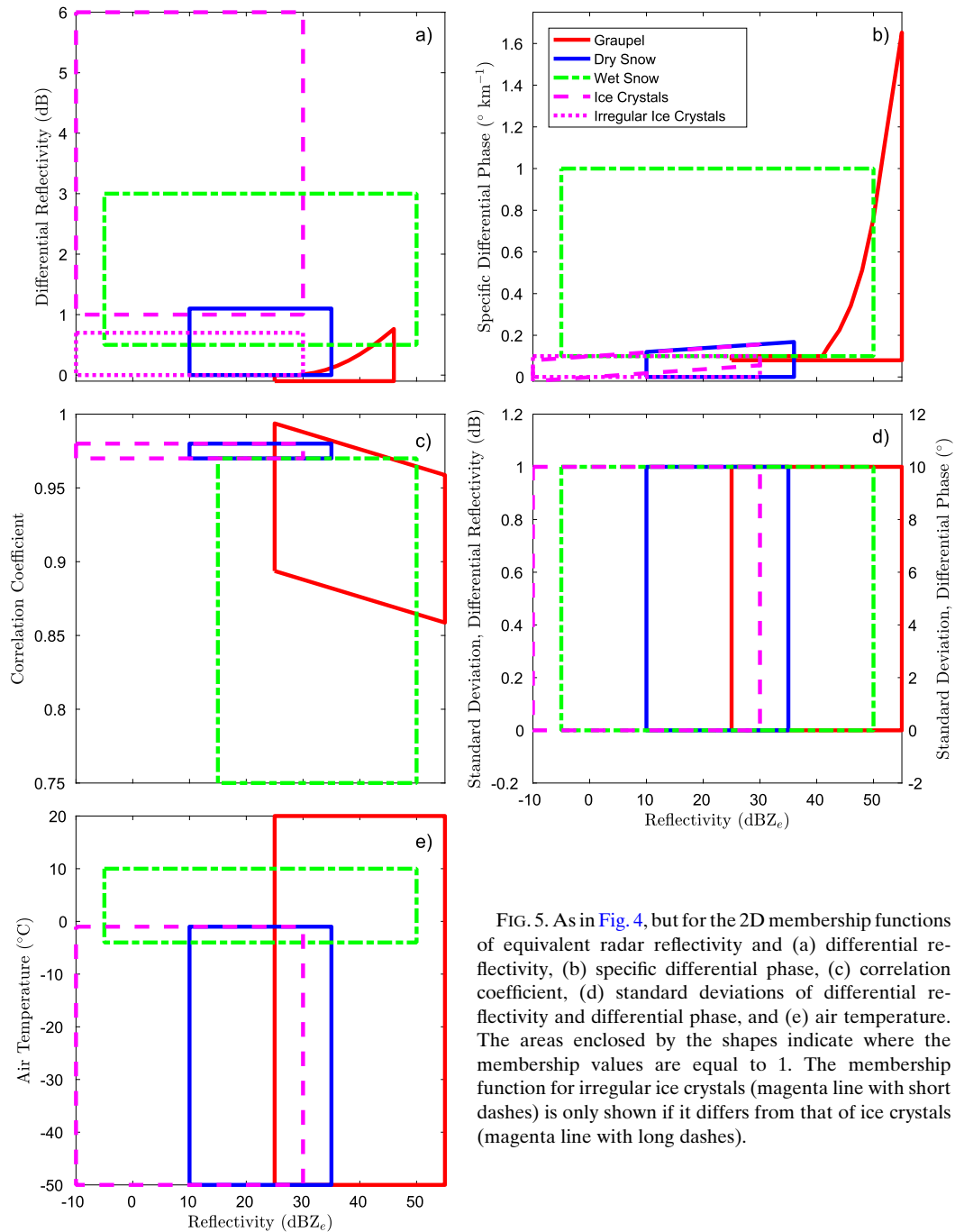
FIG. 5. As in Fig. 4, but for the 2D membership functions of equivalent radar reflectivity and (a) differential reflectivity, (b) specific differential phase, (c) correlation coefficient, (d) standard deviations of differential reflectivity and differential phase, and (e) air temperature. The areas enclosed by the shapes indicate where the membership values are equal to 1. The membership function for irregular ice crystals (magenta line with short dashes) is only shown if it differs from that of ice crystals (magenta line with long dashes).

The $h = 2$ km slice was created solely to apply the Steiner et al. (1995) convective–stratiform separation algorithm to the data (described below), since the algorithm only applies to data on a constant height surface. For both the volume and the slice, data (in units of mm^6 m^{-3} for Z_e and linear units for Z_{DR}) were linearly interpolated to a horizontal grid with 0.5-km spacing, except for the PID, which was interpolated using a

nearest-neighbor scheme. For the other radar variables, the value at a particular point was determined from the values at the nearest eight surrounding points.

4) CONVECTIVE–STRATIFORM SEPARATION ALGORITHM

The next step in the radar data processing was to apply the convective–stratiform separation algorithm from

Steiner et al. (1995), who verified the algorithm against vertical velocities from a dual-Doppler analysis of convective and stratiform precipitation in east-central Florida. The authors found that precipitation classified by the algorithm as convective had a broad distribution of vertical motions, with values frequently in excess of $\pm 5 \, \text{m s}^{-1}$. Precipitation classified as stratiform, in contrast, had a narrower distribution of vertical motions that was centered on $0 \, \text{m s}^{-1}$. Therefore, precipitation identified by the algorithm as stratiform, on average, satisfied the condition that vertical air motions are much less than the terminal fall velocity of snow particles ($1-3 \, \text{m s}^{-1}$) in stratiform clouds (Steiner et al. 1995).

In this study, the algorithm was applied to a horizontal slice of Z_e at $h = 2 \, \text{km}$. A given radar grid point was classified as convective if it satisfied either 1) an intensity threshold ($Z_e \geq 42 \, \text{dB}Z_e$) or 2) a peakedness threshold, such that Z_e exceeded the background reflectivity $Z_{e,\text{bg}}$ (calculated within an 11-km radius of the grid point), by at least $\Delta Z_{e,\text{cc}}$. The threshold $\Delta Z_{e,\text{cc}}$ was specified using the formulation that originally appeared in Yuter and Houze [1997; their Eq. (B1)], given by

$$\Delta Z_{e,\text{cc}} = a \cos\left(\frac{\pi Z_{e,\text{bg}}}{2b}\right), \tag{1}$$

where a and b are radar-specific parameters that must be tuned. Here, $a = 19 \, \text{dB}$ and $b = 56 \, \text{dB}Z_e$ were chosen because they resulted in the most consistent classification of brightband precipitation as stratiform, the same rationale used by Steiner et al. (1995) and Yuter and Houze (1997) to select their values. Once all convective centers were identified, grid points surrounding those centers were classified as convective if they fell within an intensity-dependent radius R (in km) of the centers:

$$R = \begin{cases} 0.5, & Z_{e,\text{bg}} < 20 \, \text{dB}Z_e \\ 0.5 + 3.5 \left(\dfrac{Z_{e,\text{bg}} - 20}{15}\right), & 20 \leq Z_{e,\text{bg}} < 35 \, \text{dB}Z_e \\ 4, & Z_{e,\text{bg}} \geq 35 \, \text{dB}Z_e \end{cases} \tag{2}$$

The specific values of the coefficients in this function are grid-resolution dependent (Steiner et al. 1995; Didlake and Houze 2009). We experimented with several different sets of values before selecting those of Didlake and Houze (2009), who also examined radar data on a 0.5-km grid in a TC. Nonconvective precipitation was then classified as either stratiform ($Z_e \geq 20 \, \text{dB}Z_e$) or weak echo ($Z_e < 20 \, \text{dB}Z_e$), as in Didlake and Houze (2009).
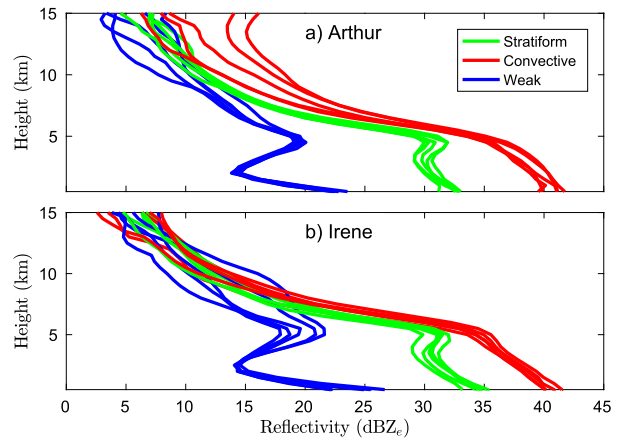

FIG. 6. Domain-averaged vertical profiles of equivalent radar reflectivity in Hurricanes (a) Arthur and (b) Irene for stratiform (green lines), convective (red lines), and weak ($Z_e < 20 \, \text{dB}Z_e$; blue lines) precipitation. Each profile represents a radar volume whose lowest elevation angle scan is shown in Fig. 1 [in (a)] and Fig. 2 [in (b)].

Domain-averaged vertical profiles of Z_e, stratified by the results of the convective–stratiform separation algorithm, are presented in Fig. 6a (Arthur) and Fig. 6b (Irene) for the radar volumes with 0.5° PPIs shown in Figs. 1 and 2, respectively. As expected, the profiles for weak-echo (blue lines) and stratiform (green lines) precipitation depict a bright band at the melting level near $h = 5 \, \text{km}$ in both storms. In contrast, there is no such signature evident in the convective profiles. That the algorithm reproduces the expected features of the Z_e profile suggests that it has been tuned properly to the WSR-88D data.

5) IWP CALCULATION

Once the convective–stratiform separation algorithm was applied, the Hogan et al. (2006) relationship was used to estimate the ice water content (IWC; g m^{-3}) in each radar grid cell that contained frozen hydrometeors:

$$\log_{10}\text{IWC} = 0.06Z_e - 0.02T - 1.7, \tag{3}$$

where T is the air temperature (°C) obtained from rawinsonde measurements at KMHX at 0600 UTC 27 August 2011 (Irene) and 0000 UTC 4 July 2014 (Arthur) within the TC environment. This empirical relationship was derived for 3-GHz (i.e., S-band) radar measurements using a large midlatitude aircraft dataset that consisted of over 10 000 in situ size spectra measured in ice clouds from $-3°$ to $-57°$C. Using the aircraft dataset, Hogan et al. (2006) found the root-mean-square error in the retrieval in Eq. (3) to be from $+50\%$ to -33% from $-10°$ to $-20°$C, increasing to from $+100\%$ to -50% at temperatures colder than $-40°$C. Matrosov (2015)

applied Eq. (3) to cross sections of WSR-88D data that were collocated with *CloudSat* transects to estimate IWP in 12 predominantly stratiform precipitation events. The results were within 50%–60% of the retrievals from *CloudSat* and were consistent with the IWP retrieval uncertainty and the range of the various IWP estimates from different *CloudSat* products. IWP estimates retrieved from *CloudSat* in Hurricanes Ike and Gustav (Matrosov 2011) were comparable to the values shown in Matrosov (2015). Unfortunately, no coincident *CloudSat* overpasses occurred in Irene or Arthur. We recognize that there may be some differences in the dependence of IWC on Z_e and air temperature between midlatitude and tropical environments, and that other IWC relations have been derived that incorporate dual-polarization radar data (e.g., Ryzhkov et al. 1998). However, we chose Eq. (3) to estimate IWC because of the large in situ aircraft dataset used to derive it and the substantial increase in the accuracy of IWC estimates that results from retrievals that include air temperature information (Liu and Illingworth 2000; Hogan et al. 2006).

Once IWC estimates were obtained, the IWC was vertically integrated to obtain the IWP, similar to the technique described by Matrosov (2015). Unlike in Matrosov (2015), however, the integration was performed separately for small (ice crystals) and large (snow and graupel) ice particles. Within each vertical column of radar data, we multiplied the IWC estimates by the thickness (in meters) of the 3-dB vertical beamwidth (0.92° for KMHX) of the elevation angle scan that contained the estimate. To avoid double counting estimates from vertically overlapping radar beams, we subtracted from the total IWP an amount equal to the average of the IWCs from the two overlapping beams multiplied by the thickness of the overlap, as suggested by Matrosov (2015). Similarly, we accounted for vertical gaps between radar beams by adding an amount equal to the average of the IWCs from the two adjacent radar beams multiplied by the thickness of the gap. While a single radar grid cell could only contribute IWP to one set of ice particles (i.e., small or large), each vertical column contained several different hydrometeor classes. Therefore, for each vertical column of radar data, we obtained two separate IWPs: that of small ice particles (i.e., regular and irregular ice crystals, hereafter referred to as the small-particle IWP) and that of large ice particles (i.e., dry and wet snow and graupel, hereafter referred to as the large-particle IWP). In the results that follow, we only considered IWP estimates between 45 and ~145 km of KMHX. Inside 45-km range, the steepest elevation angle (19.5°) scan was below 15-km height, and the IWP estimate likely would have been too small. Beyond ~145-km range, IWP was not calculated
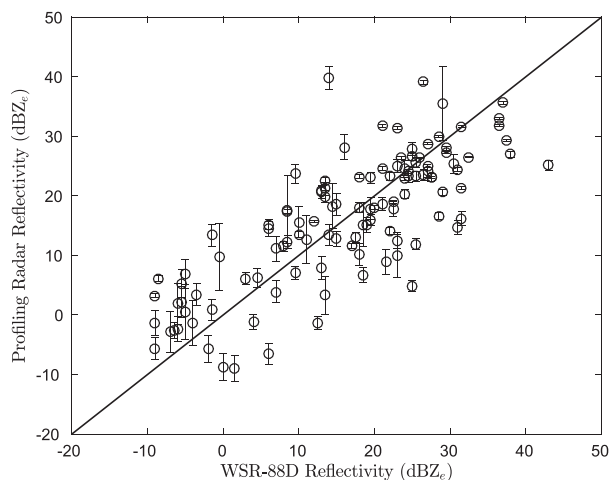

FIG. 7. Scatterplot of the equivalent radar reflectivities measured by the WSR-88D and S-PROF. Each open circle represents an individual WSR-88D Z_e measurement from the radar range gate at 0.5° elevation angle that contained S-PROF, paired with the mean of the S-PROF Z_e measurements made within the WSR-88D volume. Error bars represent the 95% confidence interval for S-PROF's mean Z_e measurement. The one-to-one line is shown.

because dual-polarization radar data were not available to separate IWP into contributions from small and large particles and the large vertical beamwidth (>2.4 km) was excessive.

b. Vertically pointing radar in New Bern, North Carolina

As part of the Hydrometeorology Testbed in the southeastern United States (HMT-Southeast), the NOAA Earth System Research Laboratory's Physical Sciences Division deployed an S-band (2.875 GHz) vertically pointing radar (S-PROF; White et al. 2000) in New Bern, North Carolina, in 2013 (Matrosov et al. 2016). S-PROF was located 37 km to the northwest of KMHX (Fig. 3) and operated from 26 June 2013 to 5 November 2015. During Hurricane Arthur, S-PROF collected Z_e and vertical Doppler velocity data over ~11 rainy hours. These data were collected every ~80 s at a vertical resolution of 60 m from 0.142- to 10.042-km height. The precipitation observed by S-PROF was primarily from the outer rainbands and the edge of the central dense overcast (Fig. 1; black square represents the location of S-PROF). To demonstrate that S-PROF and KMHX Z_e were in reasonable agreement during the event, the WSR-88D radar gate that contained S-PROF was identified and the Z_e measurements made by both radars were compared. Figure 7 shows the results of this comparison at the lowest elevation angle (0.5°), corresponding to a radar center beam height of 391 m AGL. While substantial scatter exists (standard

deviation = 8.0 dB), which is to be expected in the rapidly evolving hurricane environment, the mean disagreement in the two Z_e measurements is only 0.05 dB. The correlation coefficient for the two datasets is $r = 0.78$. Similar agreement was found at higher elevation angles (not shown).

The primary advantage of S-PROF over the WSR-88D is its observations of the fall velocity of hydrometeors (or other scatterers, in nonprecipitating conditions), which can be deduced from the vertical Doppler velocity measurements. To combine this estimate of the hydrometeor fall velocity with the polarimetric data from KMHX, each WSR-88D scan was first paired with the profile from S-PROF that was measured closest in time to the WSR-88D scan. S-PROF Z_e and Doppler velocity were then stratified by the output from the PID for the KMHX radar gate that contained S-PROF. Since the vertical resolution of the S-PROF data (60 m) far exceeded the WSR-88D vertical resolution ($\sim$595 m) corresponding to the 3-dB beamwidth at the S-PROF location, multiple S-PROF measurements were obtained within a single WSR-88D measurement volume. These observations were not averaged; instead, all S-PROF data were assigned the PID of the WSR-88D measurement volume that contained them. We did not attempt to remove vertical air motions from the S-PROF Doppler velocity data. While these vertical motions likely broadened the fall velocity distributions presented in section 4a, we expect the vertical air motions to cancel on average over an 11-h period of data collection, leaving the means of the fall velocity distributions mostly unchanged. Protat and Williams (2011) found that in tropical ice clouds, the mean profile of the vertical air velocity consisted of small values, with peaks of $\pm 0.15 \mathrm{~m~s}^{-1}$. A range in fall velocity of $0.3 \mathrm{~m~s}^{-1}$ accounts for only $\sim$7% of the range in fall velocity in our dataset, suggesting that the great majority of the variation in the fall velocity is due to its relationship with hydrometeor mass.

4. Results

a. Radar reflectivity and hydrometeor fall velocities in Hurricane Arthur

We first examine probability density functions (PDFs) of S-PROF Z_e (Fig. 8a) and hydrometeor fall velocity (v; Fig. 8b) in Hurricane Arthur. The PDFs are stratified by frozen hydrometeor class, as inferred by the WSR-88D PID [section 3a(2)], with regular and irregular ice crystals combined into the same distributions. PID classifications from 148 WSR-88D volume scans are used in the stratification, and the S-PROF data consist of 2291 pairs of Z_e and v collected during $\sim$11 rainy hours
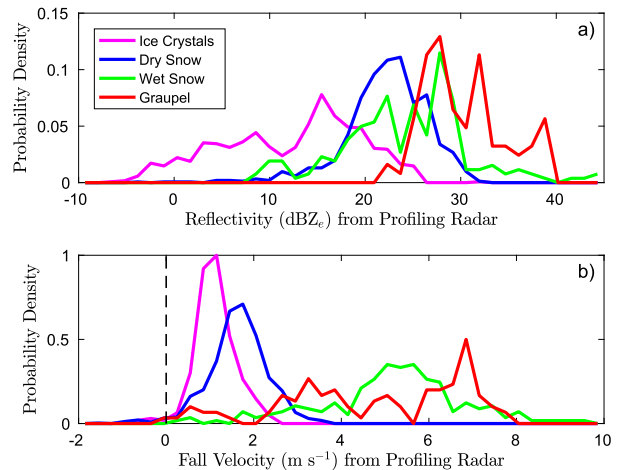

FIG. 8. PDFs of (a) equivalent radar reflectivity and (b) hydrometeor fall velocity for ice crystals (magenta lines), dry snow (blue lines), wet snow (green lines), and graupel (red lines), as derived from the S-PROF measurements in Hurricane Arthur. The dashed black line in (b) separates positive (i.e., toward the surface) and negative (i.e., away from the surface) fall velocities.

at S-PROF; 887 of these pairs are from ice crystals (purple lines), 1114 from dry snow (blue lines), 190 from wet snow (green lines), and 100 from graupel (red lines). As expected, the PDFs in Fig. 8 demonstrate that as hydrometeors transition from small-diameter ice crystals to aggregated dry snowflakes and finally to the heaviest particles (wet snow and rimed graupel), Z_e and v both increase. Although the ice crystals have the slowest v, nearly all of the ice crystals observed here were descending (with mean $v \sim 1 \mathrm{~m~s}^{-1}$). While TC anvils may contain smaller ice crystals with slower terminal fall velocities, this analysis suggests that the WSR-88D is not sensitive enough to detect such particles. At 37 km (the distance between KMHX and S-PROF), the smallest WSR-88D measurement of Z_e made above the melting layer was $-9 \mathrm{~dB} Z_e$. It is also possible that at altitudes greater than 10 km (above the maximum height of the S-PROF profiles), the WSR-88D observed ice crystals that fell more slowly than those shown in Fig. 8b, but this cannot be determined from the current dataset. These limitations must be considered when interpreting the results that follow.

In section 4b, we will use the WSR-88D data and the PID output to separate ice hydrometeors into two groups: small ice (i.e., ice crystals) and large ice (i.e., dry snow, wet snow, and graupel). We will then calculate the ice water path for each of the two groups of hydrometeors. For the purpose of computing accurate small- and large-particle IWPs, it is acceptable to misclassify the large ice particles as an incorrect large ice species (e.g., to mistake wet snow for graupel), but it is not acceptable
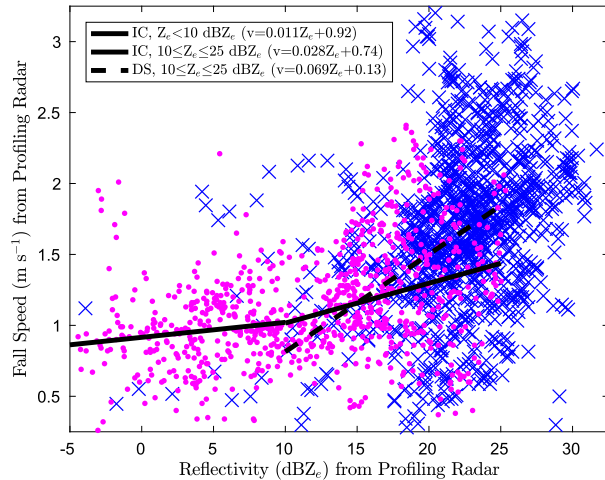
FIG. 9. Scatterplot of equivalent radar reflectivity and hydrometeor fall velocity of ice crystals (magenta dots) and dry snow (blue crosses) measured by S-PROF in Hurricane Arthur. The lines indicate the least squares linear regression between equivalent radar reflectivity and fall velocity for ice crystals (black solid line for $Z_e < 10\,\mathrm{dB}Z_e$ and $10 \leq Z_e \leq 25\,\mathrm{dB}Z_e$) and dry snow (black dashed line; $10 \leq Z_e \leq 25\,\mathrm{dB}Z_e$).

to mistake small ice particles (i.e., ice crystals) for large ones, such as dry snowflakes. The distributions in Fig. 8b demonstrate that particles classified as ice crystals and dry snow overlap considerably in their fall velocities, leaving us to wonder whether the PID is capable of distinguishing between these two types of particles in a mean sense. Before we calculate small- and large-particle IWPs, we must investigate whether this misclassification is likely to have occurred.

Figure 9 is a scatterplot that shows the relationship between Z_e and v for ice crystals (magenta dots) and dry snow (blue crosses). Each point represents an individual S-PROF measurement of Z_e and v made within a WSR-88D volume. All 2001 observations of ice crystals and dry snow (~11 h of matched S-PROF and WSR-88D data) are shown without any averaging or filtering. Although v is height dependent, no attempt has been made to normalize the observed v to a specific height, since this normalization depends on crystal habit and rime fraction (Heymsfield 1972), which are unknown. While there are regions of the scatterplot that are dominated by only one ice species, the interior of the diagram ($10 \leq Z_e \leq 25\,\mathrm{dB}Z_e$) consists of some overlap. This is the region of the parameter space in which misclassifications are most likely to occur. To determine whether the PID algorithm classified these particles into two microphysically distinct groups, the slopes of the two best-fit lines for dry snow and ice crystals within the region of overlap ($10 \leq Z_e \leq 25\,\mathrm{dB}Z_e$) were calculated. Within this region, the slope of the best-fit line for ice

crystals (solid line in Fig. 9 where $10 \leq Z_e \leq 25\,\mathrm{dB}Z_e$) is $0.028\,\mathrm{dB}Z_e^{-1}$, while the slope of the best-fit line for dry snow (dashed line in Fig. 9) is $0.069\,\mathrm{dB}Z_e^{-1}$. The difference in the slopes is statistically significant at the 99% level ($p = 0.00002$), which supports the notion that the two sets of particles have different mass–diameter relationships and thus have different microphysical properties. Further, the difference in the slopes of the best-fit lines for ice crystals with $Z_e < 10\,\mathrm{dB}Z_e$ ($0.011\,\mathrm{dB}Z_e^{-1}$) and ice crystals with $10 \leq Z_e \leq 25\,\mathrm{dB}Z_e$ ($0.028\,\mathrm{dB}Z_e^{-1}$) is not statistically significant at the 99% level ($p = 0.03$). Together, these results suggest that the particles classified as ice crystals by the PID have statistically similar mass–diameter relationships, independent of their reflectivity, which differ from those of the particles classified as dry snow. Partial riming of the dry snow particles may explain why their fall velocity increases at a faster rate (per unit Z_e) than that of the ice crystals, and differing amounts of riming (together with varying vertical air motions) may explain the large variation in the fall velocity of dry snow for a given Z_e (Locatelli and Hobbs 1974). In summary, this analysis suggests that the PID is capable of distinguishing between the two ice species in a mean sense, which provides support for calculating small- and large-particle IWPs. Nevertheless, the following results are predicated on the accuracy of the PID, and this remains a source of uncertainty.

b. IWPs in Hurricane Arthur (2014)

Figure 1 shows the five PPIs of Z_e from the WSR-88D that are representative of the 6-h period surrounding Arthur's landfall in North Carolina. The black lines superimposed on the Z_e field enclose areas of active convection, as identified by the Steiner et al. (1995) convective–stratiform separation algorithm [section 3a(4)]. In general, the PPIs depict a well-organized, mature hurricane with a symmetric precipitation distribution. Convection was particularly active in both the principal rainband (labeled A in Figs. 1a,b) north of the center and in the eastern eyewall (labeled W in Fig. 1).

From Eq. (3), the WSR-88D Z_e, the temperature profile from the 0000 UTC 4 July 2014 sounding at KMHX, and the method described in section 3a(5), IWP (Fig. 10) was estimated for each of the five volume scans whose PPIs are shown in Fig. 1. Because the predominant features in each IWP map are similar, we will use the IWP map from 2340 UTC 3 July 2014 (Fig. 10a) as an example of the IWP characteristics present in each of the radar scans. Figure 10a depicts three distinct areas of Hurricane Arthur from an IWP perspective: 1) a convective principal rainband (labeled A) that contains IWP $> 5\,\mathrm{kg\,m^{-2}}$ within its core, surrounded by smaller IWP of 1–$2\,\mathrm{kg\,m^{-2}}$ along its periphery; 2) the "moat"
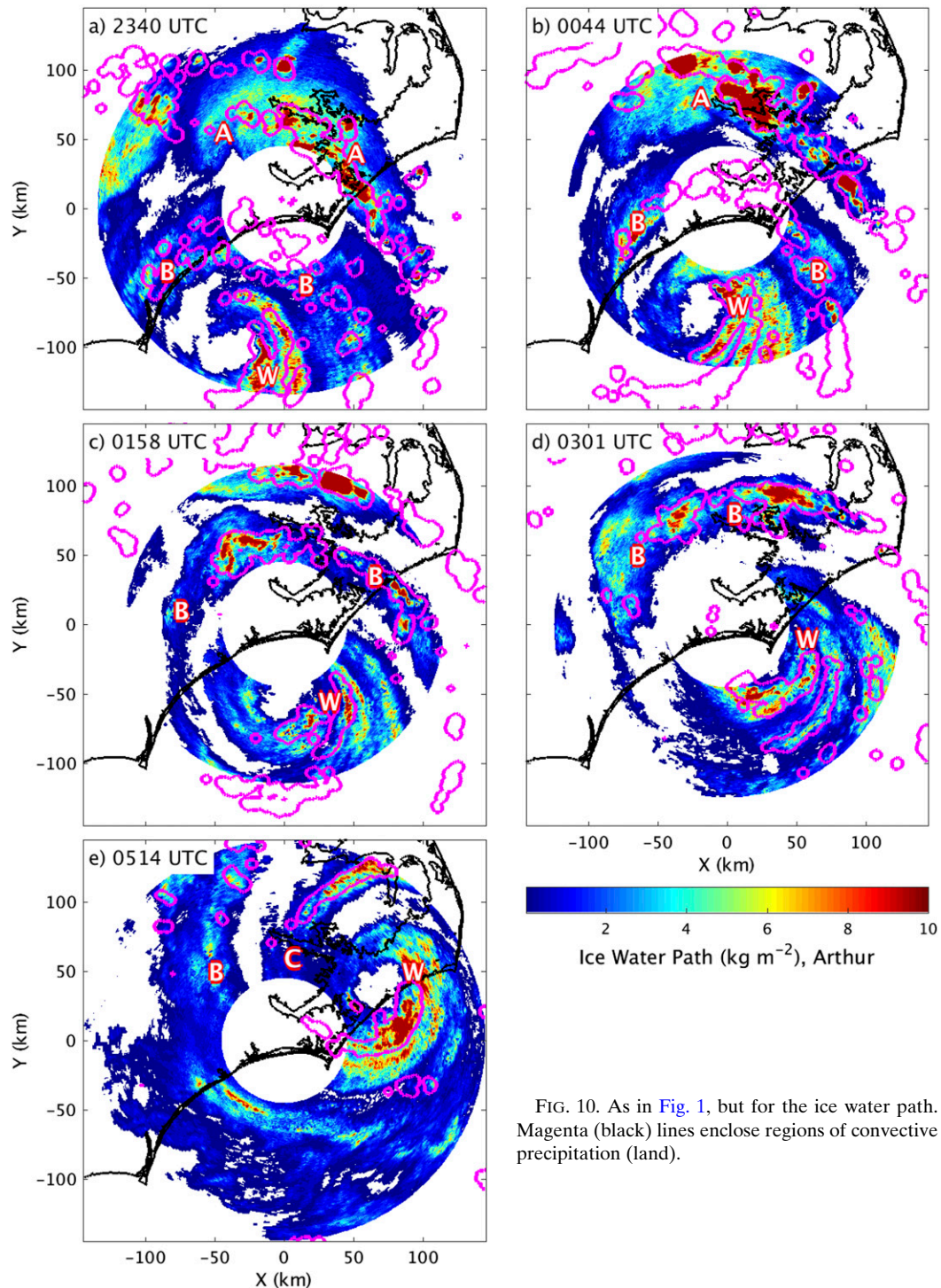
FIG. 10. As in Fig. 1, but for the ice water path. Magenta (black) lines enclose regions of convective precipitation (land).

region between the principal rainband and the eyewall (labeled W), which contains stratiform rain and shallow convective rainbands (labeled rainband B in Figs. 10a,b and rainband C in Fig. 10e) and mostly consists of IWP $< 5\,\mathrm{kg\,m^{-2}}$; and 3) the eyewall, which is convective

and contains $Z_e > 45\,\mathrm{dB}Z_e$ (Fig. 1a) and IWP $> 5\,\mathrm{kg\,m^{-2}}$. In general, the largest IWP values ($>8\,\mathrm{kg\,m^{-2}}$) occur within regions of active convection within the principal rainband and the eyewall, where updrafts have lofted an appreciable amount of snow (and some graupel) into the
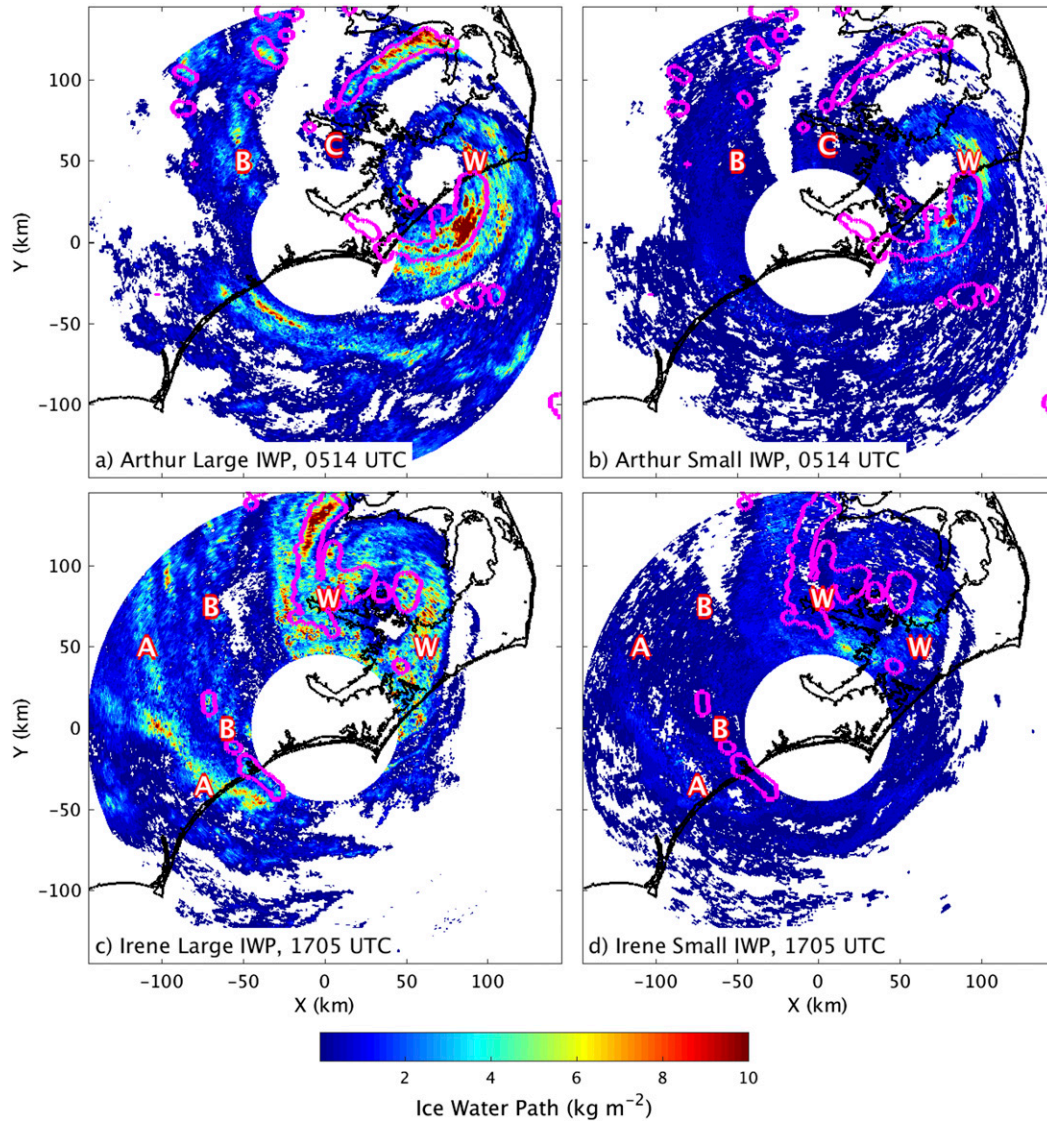
FIG. 11. As in Fig. 10, but for (a),(c) large and (b),(d) small ice water paths in Hurricanes (top) Arthur at 0514 UTC 4 Jul 2014 and (bottom) Irene at 1705 UTC 27 Aug 2011.

column, capped by unaggregated ice crystals above $h \sim 7$ km. The larger IWP values (8–10 kg m^{-2}) within these regions are consistent with WSR-88D estimates of IWP in heavier stratiform precipitation (Matrosov 2015) and those estimated from *CloudSat* overpasses of Hurricanes Ike and Gustav (Matrosov 2011). In contrast, the region of stratiform rain and shallow convective rainbands that lies between the principal rainband and the eyewall contains IWP < 5 kg m^{-2} because the weak convection in this area does not generate substantial amounts of small or large ice, although ice crystals still enter this area as they are ejected radially outward from the upper portion of the eyewall by the secondary circulation. The rainbands in this region (B and C in

Fig. 10) appear similar to the low-topped rainbands noted by May et al. (2008) in the moat of TC Ingrid. The shallow nature of these rainbands is not readily apparent from PPIs of Z_e at the lowest elevation angle of 0.5° (Fig. 1), but is obvious from vertically integrated quantities like IWP.

The relative contributions of the two ice classes to the total IWP can be further investigated through the small-particle (i.e., ice crystal) IWP (Fig. 11a) and large-particle (i.e., snow and graupel) IWP (Fig. 11b) plan plots shown in Fig. 11. Figures 11a and 11b provide an example of these estimates from one radar volume scan at 0514 UTC. The spatial patterns in the total IWP (Fig. 10e) tend to be dominated by those of the large-particle IWP (Fig. 11a).
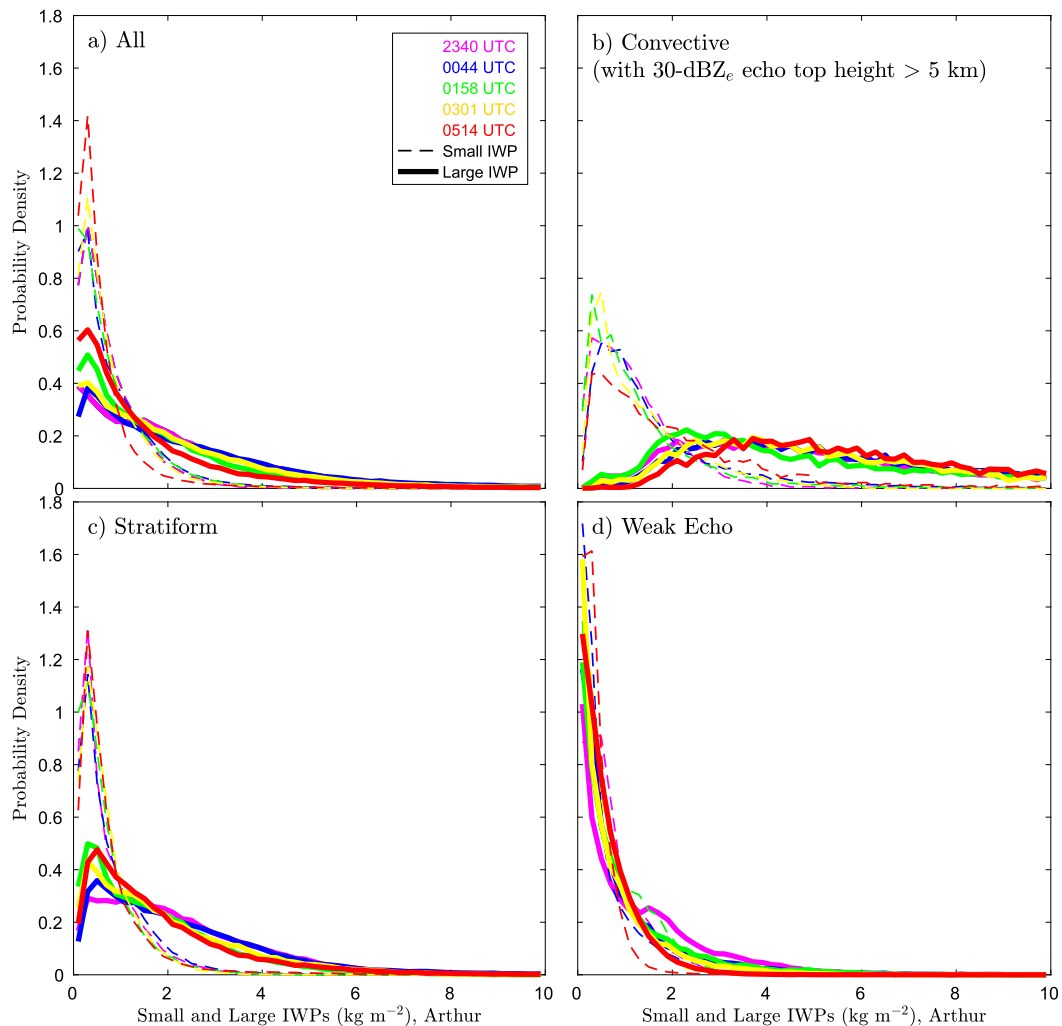
FIG. 12. PDFs of the small (dashed lines) and large (solid lines) ice water paths for (a) all, (b) convective (with 30-dBZ_e echo-top height > 5 km), (c) stratiform, and (d) weak precipitation at 2340 (magenta lines), 0044 (blue lines), 0158 (green lines), 0301 (yellow lines), and 0514 (red lines) UTC 3–4 Jul 2014 in Hurricane Arthur.

This result is not surprising, given that dry snow makes up a substantial portion of the TC ice mass (Black and Hallett 1986). Like the total IWP, the largest values of large-particle IWP reside within regions of active convection (enclosed by magenta lines), where upward motion contributes to the most efficient dendritic growth, aggregation of snowflakes, and localized areas of riming to form graupel. The smallest large-particle IWP values (<2 kg m^{-2}) are located almost exclusively in stratiform precipitation. While small-particle IWP (Fig. 11b) makes up a much smaller percentage of the total IWP in most areas, there is nevertheless a distinctive spatial pattern in the small-particle IWP as well. As in the large-particle IWP, the small-particle IWP field has localized maxima (up to 4 kg m^{-2}) in the eyewall (labeled W), an area with cold cloud tops

conducive to ice crystal formation. Outside the convection, there are broad areas of small-particle IWP of 1–2 kg m^{-2}, which demarcate the anvil region of the TC. Although not shown, characteristics similar to those discussed above are present in estimates from the other radar volume scans.

Figure 12 presents probability density functions of the small (thin dashed lines) and large (thick solid lines) particle IWPs. The colors in Fig. 12 denote the five radar scans (Fig. 1), and distributions from all precipitation (Fig. 12a), highly convective regions with 30-dBZ echo-top heights > 5 km (Fig. 12b), stratiform precipitation (Fig. 12c), and weak precipitation with $Z_e < 20$ dBZ_e at $h = 2$ km (Fig. 12d) are presented. When all precipitation is considered (Fig. 12a), both the small and large IWPs peak around ~0.5 kg m^{-2}, but the small ice
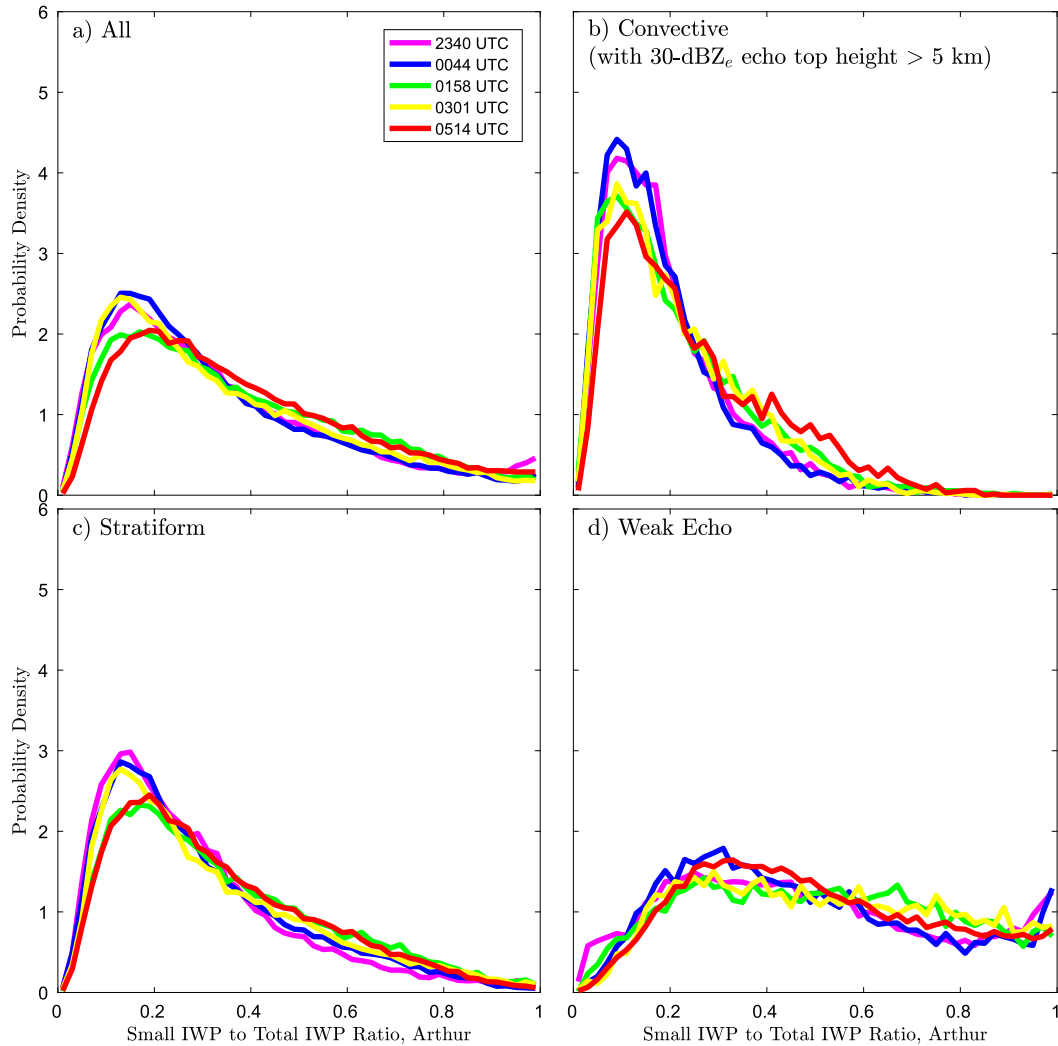
FIG. 13. As in Fig. 12, but for the small-to-total IWP ratio.

distribution is much narrower than that of the large ice. In highly convective conditions (i.e., convective areas with 30-dBZ echo-top heights > 5 km; Fig. 12b), both distributions are skewed to the right and the peak of the large ice distribution increases from 0.5 to 2–4 kg m^{-2}, reflecting the increased quantities of all ice species, especially snow and graupel, generated by intense convection. If the echo-top height criterion were removed (not shown), the convective distributions would be similar to those for all precipitation, as the shallow, limited ice-producing convection between the principal rainband and eyewall would dominate the convective IWP distributions. If larger thresholds for echo-top height (i.e., a greater reflectivity or height) were chosen, both the small and large IWP distributions would shift toward larger values, reflecting the increased amounts of ice that the most intense convection can produce. Conversely, when only stratiform precipitation is considered (Fig. 12c), the distributions resemble those from all precipitation, primarily because stratiform precipitation makes up a majority of the precipitation analyzed here. Finally, if only weak precipitation ($Z_e < 20$ dBZ_e at $h = 2$ km) is considered (Fig. 12d), both the small and large IWP distributions appear similar, with peaks near 0.1 kg m^{-2} and tails that decrease to near-zero density from 2 to 5 kg m^{-2}. The weak precipitation class is the only precipitation type examined here that has similar small and large IWP distributions, primarily due to the reduced quantity of large ice particles in these regions.

We now extend this analysis by computing the ratio of the small IWP to the total IWP. Distributions of this IWP ratio (Fig. 13) indicate the relative contribution of ice crystals to the total IWP in the different precipitation
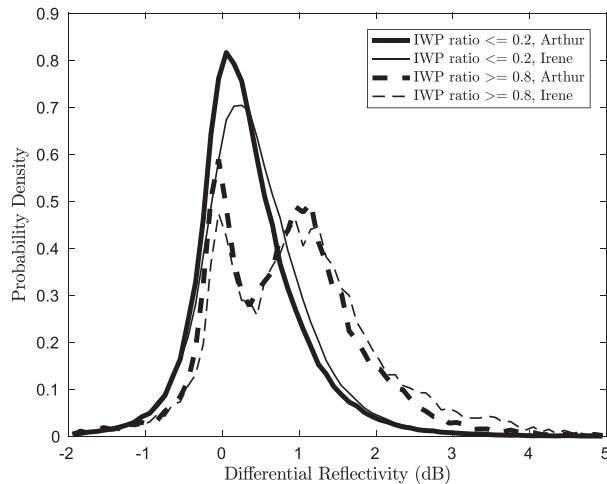
FIG. 14. PDFs of the differential reflectivity above the melting layer for regions of small-to-total IWP ratio ≤ 0.2 (solid lines) and ≥ 0.8 (dashed lines) in Hurricanes Arthur (thick lines) and Irene (thin lines).

regimes described above. In Figs. 13a–c, the IWP ratios have gammalike distributions, similar to those of ice particle size. The most common values of the IWP ratio range from 0.1 to 0.2 for the first three sets of distributions (Figs. 13a–c), with most of the all and stratiform precipitation distributions peaking around 0.15 and most of the highly convective precipitation distributions peaking around 0.1. These highly convective distributions are narrower than any of the other sets of distributions, with few areas in which more than 60% of the IWP is contributed by ice crystals. In contrast, the weak-echo regions ($Z_e < 20 \, \mathrm{dB}Z_e$) contain the broadest IWP ratio distributions (Fig. 13d). In these regions, the peak probability density occurs at larger IWP ratios (0.25–0.35; Fig. 13d) than in the other precipitation regimes (0.1–0.2; Figs. 13a–c). In addition, only the weak-echo regions contain substantial probability density at large IWP ratios (>0.8), and two of the weak-echo distributions are even bimodal, with a secondary maximum near unity. Within the weak-echo regions ($Z_e < 20 \, \mathrm{dB}Z_e$), snow and graupel are sparse enough that IWP from ice crystals is comparable to (or even exceeds) the contribution from larger ice species.

To provide some evidence that unaggregated ice crystals are present above the melting layer in regions with large IWP ratios, Z_{DR} values for all radar gates classified as dry snow, graupel, and ice crystals in the five radar scans shown in Fig. 1 were combined and stratified by IWP ratio ≤ 0.2 (thick solid line in Fig. 14) and IWP ratio ≥ 0.8 (thick dashed line in Fig. 14). Since dry snow and graupel particles have less bulk density and are more spherical than ice crystals, regions with large Z_{DR}

values above the melting layer are likely to consist mostly of unaggregated ice crystals. Indeed, while the Z_{DR} distribution for IWP ratios ≤ 0.2 (thick solid line in Fig. 14) is singularly peaked near 0 dB, the Z_{DR} distribution for IWP ratios ≥ 0.8 (thick dashed line in Fig. 14) is bimodal, with a secondary peak near 1.1 dB and a much longer right tail that extends to 4 dB. This Z_{DR} distribution suggests that ice crystals contribute substantially to the radar signal above the melting layer when the IWP ratio is greater than or equal to 0.8.

c. IWPs in Hurricane Irene (2011)

The IWP maps of Hurricane Irene (Fig. 15) reveal many of the same characteristics as in Arthur. The principal rainband (labeled A in Figs. 2 and 15) and the eyewall (labeled W) contain the most consistently large IWP values (locally exceeding $10 \, \mathrm{kg \, m^{-2}}$) over time. This is despite the fact that the principal rainband contains little active convection (areas enclosed by magenta lines). Similar to Arthur, the shallow rainband labeled B in Figs. 2 and 15 is located within the moat between the principal rainband and the convection close to the eyewall, and this rainband contains IWPs mostly less than $5 \, \mathrm{kg \, m^{-2}}$ throughout the period of study. The IWP associated with rainband C is initially comparable to that of the principal rainband at 0832 UTC (Fig. 15a) and 0938 UTC (Fig. 15b). However, it later weakens and disperses as it moves away from the eyewall and into the moat region from 1438 to 1536 UTC (Figs. 15c,d), eventually becoming indistinguishable from rainband B at 1705 UTC (Fig. 15e).

The separation of the IWP into that contributed by large particles (Fig. 11c) and small particles (Fig. 11d) at 1705 UTC reveals that enhanced amounts of small and large ice are primarily confined to the principal rainband (A) and the eyewall (W). There is almost no small- or large-particle IWP $> 5 \, \mathrm{kg \, m^{-2}}$ in rainband B, owing to its shallow nature. When the small and large IWP distributions are examined (Fig. 16), the characteristics are similar to those in Arthur and include 1) similar distributions in all (Fig. 16a) and stratiform (Fig. 16c) precipitation, 2) large IWP distributions skewed toward greater values in highly convective precipitation (Fig. 16b), and 3) roughly similar amounts of small and large IWP in weak precipitation (Fig. 16d).

Figure 17 presents the probability distribution functions of the IWP ratio for all (Fig. 17a), highly convective (30-$\mathrm{dB}Z_e$ echo-top heights $> 5 \, \mathrm{km}$; Fig. 17b), stratiform (Fig. 17c), and weak-echo ($Z_e < 20 \, \mathrm{dB}Z_e$; Fig. 17d) precipitation in Irene. In all but the weak-echo precipitation, these gammalike distributions peak at IWP ratios between 0.1 and 0.2. Similar to Arthur, there is
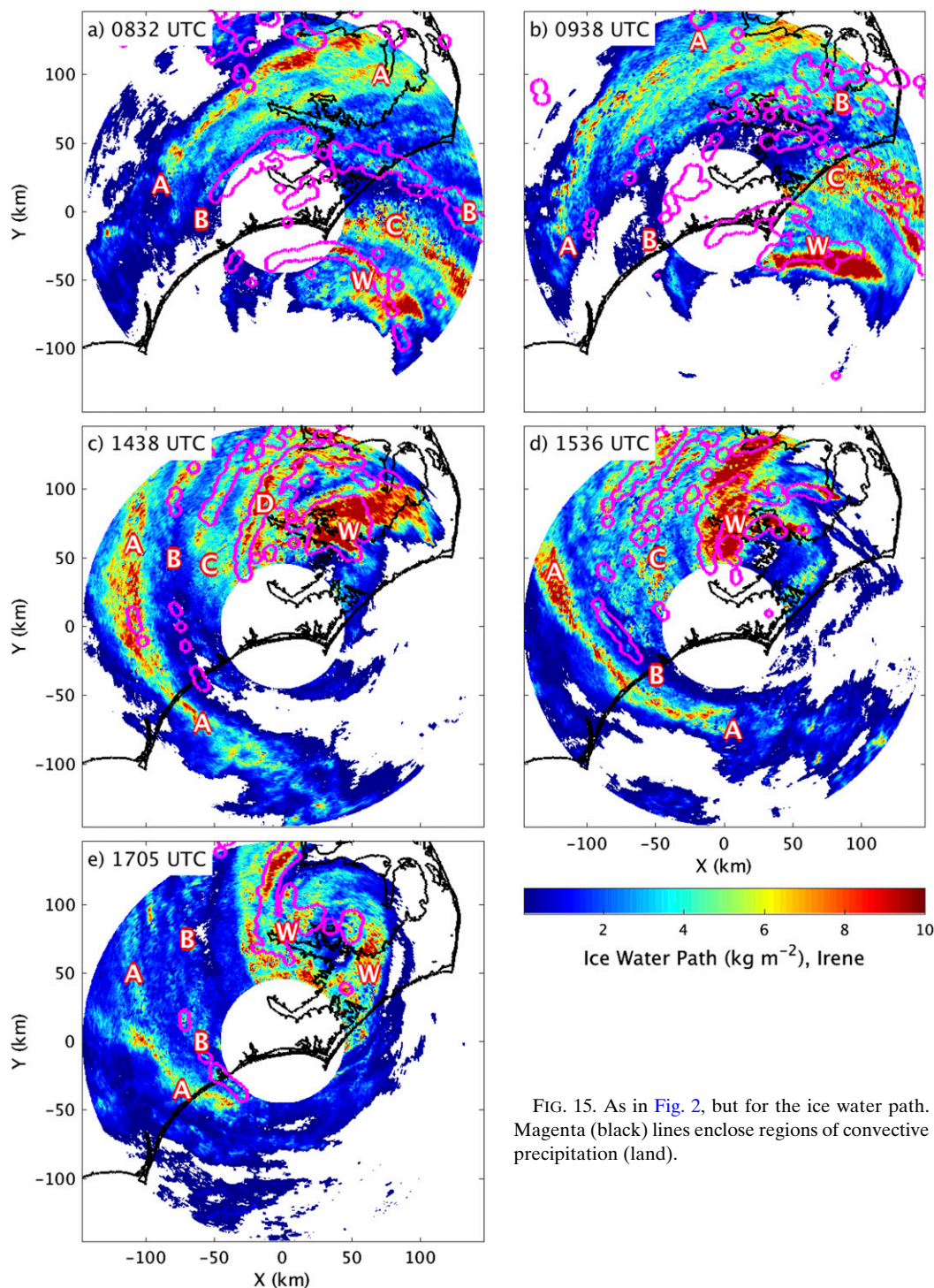
FIG. 15. As in Fig. 2, but for the ice water path. Magenta (black) lines enclose regions of convective precipitation (land).

little difference in this ratio between all (Fig. 17a) and stratiform precipitation (Fig. 17c), while highly convective precipitation (Fig. 17b) has a narrower IWP ratio distribution. IWP ratios ≥ 0.8 are mostly confined to the weak-echo regime (Fig. 17d). As in Hurricane

Arthur, these regions are characterized by some relatively large (1–4 dB) Z_{DR} values above the melting layer (thin dashed line in Fig. 14), suggestive of unaggregated ice crystals with horizontally aligned major axes.
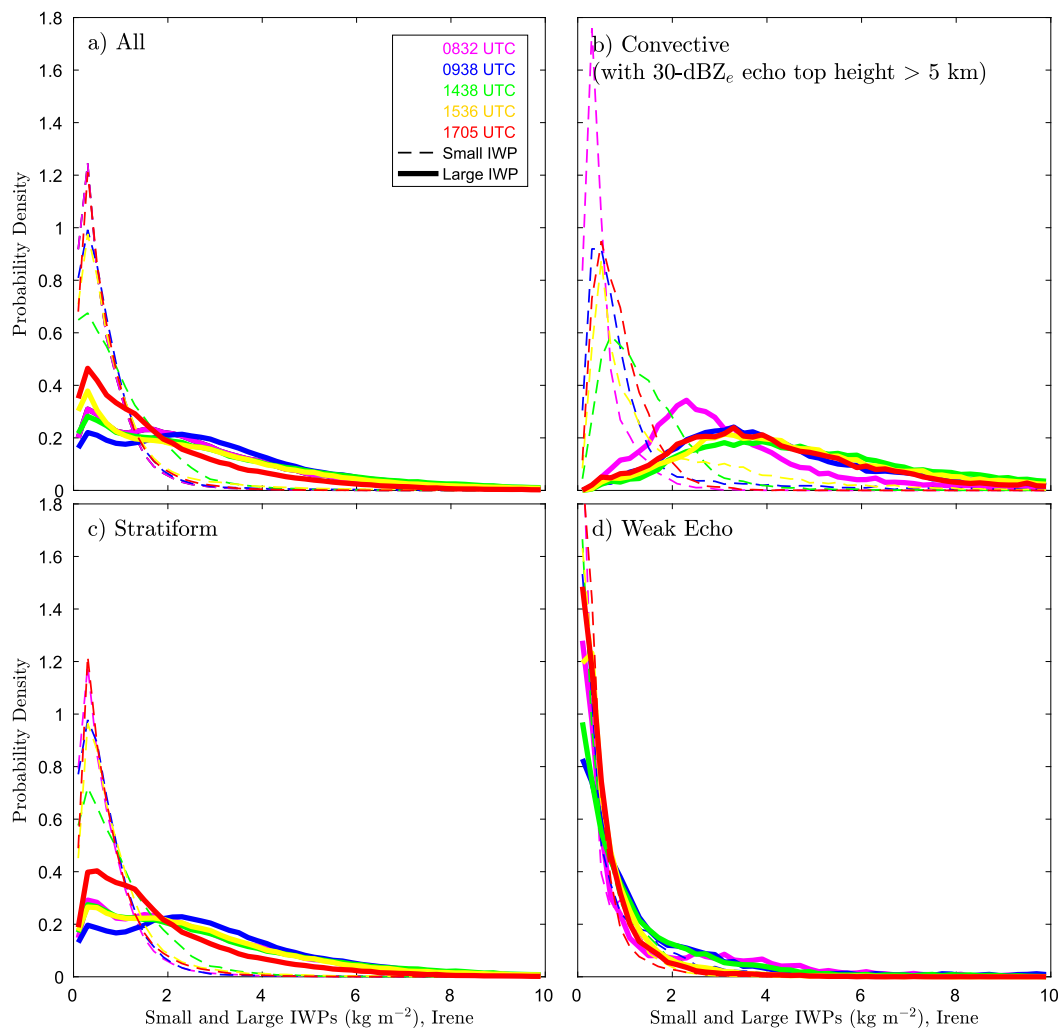
FIG. 16. As in Fig. 12, but at (a) 0832 (magenta lines), (b) 0938 (blue lines), (c) 1438 (green lines), (d) 1536 (yellow lines), and (e) 1705 (red lines) UTC 27 Aug 2011 in Hurricane Irene.

5. Discussion and conclusions

In this paper, we used data from the dual-polarization WSR-88D at KMHX and the method in Matrosov (2015) to generate IWP maps in Hurricanes Irene (2011) and Arthur (2014), using a relationship between IWC, Z_e, and air temperature [Eq. (3)] derived by Hogan et al. (2006) from a large midlatitude aircraft dataset. This is the first time that WSR-88D data have been used to estimate the two-dimensional IWP field. We then extended the Matrosov (2015) method further by using the Vivekanandan et al. (1999) hydrometeor classification algorithm to separate the IWP into the contribution from ice crystals (i.e., small-particle IWP) and the contribution from snow and graupel (i.e., large-particle IWP). The ratio of the small-to-total IWP was then calculated to quantify the relative contribution from

each set of ice species. The IWP quantities were also stratified by precipitation regime (i.e., convective, stratiform, and weak echo) using the Steiner et al. (1995) convective–stratiform separation algorithm. We also used measurements from an S-band vertically profiling radar that was located 37 km to the northwest of KMHX to quantify the fall velocity distribution of each ice species in Hurricane Arthur. These data allowed us to determine the approximate subset of ice crystals that were observed by the WSR-88D and that were included in the IWP estimates.

In general, the IWP maps revealed that the largest IWPs, which locally exceeded $10 \, \mathrm{kg \, m^{-2}}$, were located in the principal rainband and the eyewall of both hurricanes. In between these two features, a minimum in IWP was observed, with values generally below $5 \, \mathrm{kg \, m^{-2}}$. These relatively small IWP values were contained
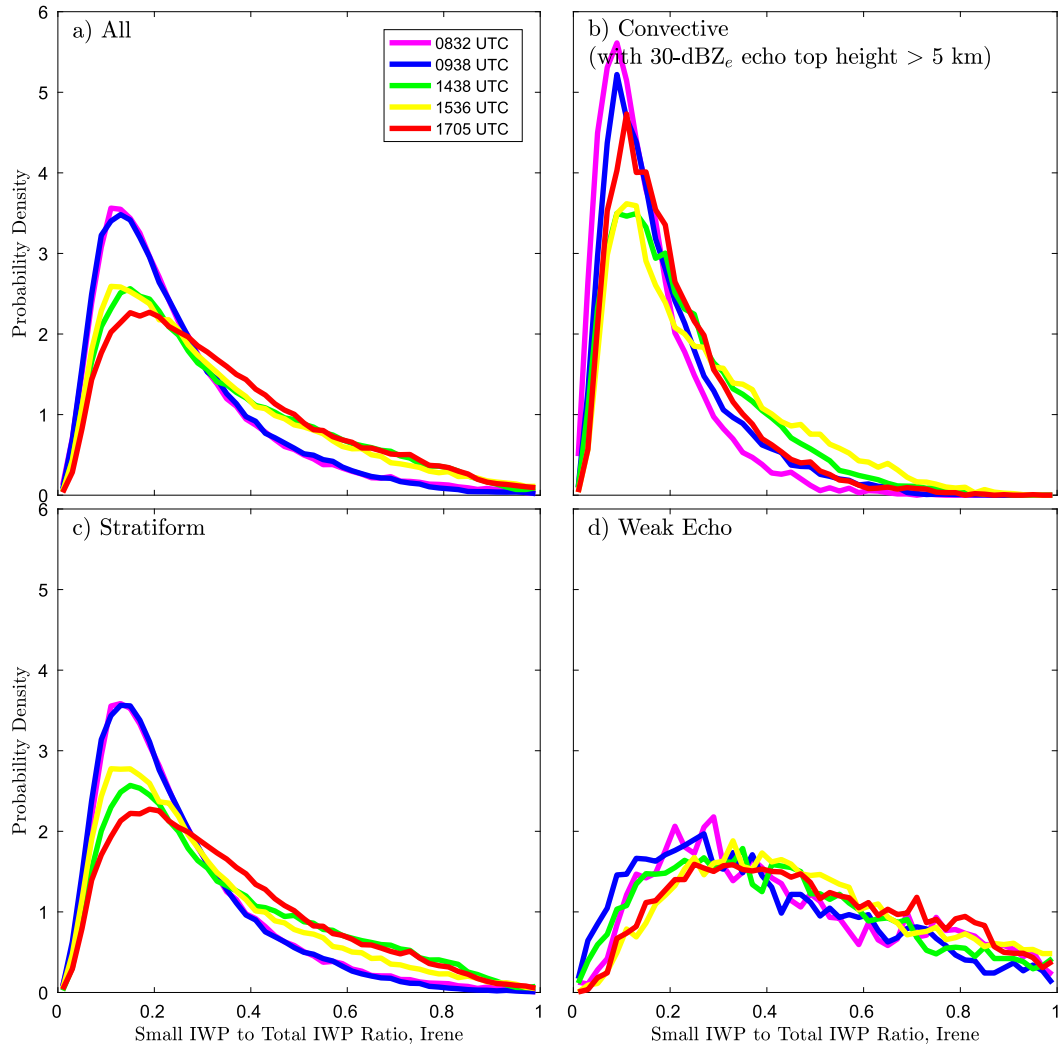
FIG. 17. As in Fig. 16, but for the small-to-total IWP ratio.

within shallow rainbands inside the moat, a region of weakly subsident air within the TC. When the total IWP was subdivided into maps of the contributions from small and large ice, we found that each of these fields generally followed the pattern shown in the total IWP field, with increased small- and large-particle IWP in the principal rainbands and the eyewall.

Probability density functions of the small-to-total IWP ratio revealed that the majority of radar grid cells contained ratios less than 0.4, with the exception of weak-echo precipitation ($Z_e < 20\,\mathrm{dB}Z_e$ at $h = 2\,\mathrm{km}$). Intense convection (convective areas with 30-dBZ_e echo-top heights $> 5\,\mathrm{km}$) had the narrowest IWP ratio distributions, with peaks near 0.1 and tails that did not extend past 0.7. Weak-echo precipitation, in contrast, had distributions that peaked near 0.3 and tails that extended to 1.0 (where a secondary peak was sometimes

located). These large IWP-ratio regions were most common along the edges of the principal rainband and within the moat, where ice crystals made up a substantial portion of the total IWP.

Because of the limited sensitivity of the WSR-88D, only a subset of the true ice crystal distribution was included in the IWP fields presented here. Fortunately, S-PROF measurements of fall velocity from Hurricane Arthur were available to quantify the portion of the ice crystal distribution below 10 km (i.e., the maximum height of the S-PROF profiles) that was detected by the WSR-88D. The distribution of ice crystal fall velocities had a peak probability density at $v = 1\,\mathrm{m\,s}^{-1}$, but the probability density decreased to less than half of its peak value at $v = 0.5\,\mathrm{m\,s}^{-1}$. Almost no ice crystals with a fall velocity smaller than $0.25\,\mathrm{m\,s}^{-1}$ were observed. It is likely that such ice crystals existed, but that they were

too small for the WSR-88D to detect and/or were located above the 10-km height limit of S-PROF. Therefore, when observed maps of small-particle IWP or distributions of the IWP ratio are compared with those from a model, care must be taken to ensure that a similar subset of ice crystals has been selected from the model for comparison. With these caveats in mind, the maps and distributions of the IWP quantities presented here may represent a valuable opportunity to evaluate directly the ice microphysical depiction of TCs in numerical weather prediction models.

Future studies may wish to examine the sensitivity of the results presented in section 4 to different relations between radar variables and IWC and to different hydrometeor classification schemes. IWC relations derived from studies of tropical convection and those that utilize dual-polarization radar data (e.g., Ryzhkov et al. 1998) may be of particular interest. These relations should be evaluated against the independent in situ aircraft measurements made in tropical cyclones above the melting layer (e.g., Black and Hallett 1986, 1999; Black 1990; Black et al. 1994, 2003; Heymsfield et al. 2006) to estimate the error associated with the chosen IWC relation(s). Finally, others may wish to apply the methods described here to different weather phenomena, such as frontal precipitation and extratropical cyclones, to estimate the two-dimensional IWPs and the small-to-total IWP ratios in those systems. Equation (3) is particularly suited for such research, given that it was derived from a midlatitude aircraft dataset collected in England.

REFERENCES

Andreae, M. O., D. Rosenfeld, P. Artaxo, A. A. Costa, G. P. Frank, K. M. Longo, and M. A. F. Silva-Dias, 2004: Smoking rain clouds over the Amazon. *Science*, **303**, 1337–1342, doi:10.1126/science.1092779.

Avila, L. A., and J. Cangialosi, 2011: Tropical cyclone report, Hurricane Irene. National Hurricane Center, National Weather Service, 45 pp. [Available online at http://www.nhc.noaa.gov/data/tcr/AL092011_Irene.pdf.]

Balakrishnan, N., and D. S. Zrnić, 1990: Use of polarization to characterize precipitation and discriminate large hail. *J. Atmos. Sci.*, **47**, 1525–1540, doi:10.1175/1520-0469(1990)047<1525:UOPTCP>2.0.CO;2.

Berg, R., 2015: Tropical cyclone report, Hurricane Arthur. National Hurricane Center, National Weather Service, 43 pp. [Available online at http://www.nhc.noaa.gov/data/tcr/AL012014_Arthur.pdf.]

Black, M. L., R. W. Burpee, and F. D. Marks Jr., 1996: Vertical motion characteristics of tropical cyclones determined with airborne Doppler radial velocities. *J. Atmos. Sci.*, **53**, 1887–1909, doi:10.1175/1520-0469(1996)053<1887:VMCOTC>2.0.CO;2.

Black, R. A., 1990: Radar reflectivity–ice water content relationships for use above the melting level in hurricanes. *J. Appl. Meteor.*, **29**, 955–961, doi:10.1175/1520-0450(1990)029<0955:RRIWCR>2.0.CO;2.

——, and J. Hallett, 1986: Observations of the distribution of ice in hurricanes. *J. Atmos. Sci.*, **43**, 802–822, doi:10.1175/1520-0469(1986)043<0802:OOTDOI>2.0.CO;2.

——, and ——, 1999: Electrification of the hurricane. *J. Atmos. Sci.*, **56**, 2004–2028, doi:10.1175/1520-0469(1999)056<2004:EOTH>2.0.CO;2.

——, H. B. Bluestein, and M. L. Black, 1994: Unusually strong vertical motions in a Caribbean hurricane. *Mon. Wea. Rev.*, **122**, 2722–2739, doi:10.1175/1520-0493(1994)122<2722:USVMIA>2.0.CO;2.

——, G. M. Heymsfield, and J. Hallett, 2003: Extra large particle images at 12 km in a hurricane eyewall: Evidence of high-altitude supercooled water? *Geophys. Res. Lett.*, **30**, 2124, doi:10.1029/2003GL017864.

Bluestein, H. B., M. M. French, R. L. Tanamachi, S. Frasier, K. Hardwick, F. Junyent, and A. L. Pazmany, 2007: Close-range observations of tornadoes in supercells made with a dual-polarization, X-band, mobile Doppler radar. *Mon. Wea. Rev.*, **135**, 1522–1543, doi:10.1175/MWR3349.1.

Bringi, V. N., and V. Chandrasekar, 2001: *Polarimetric Doppler Weather Radar: Principles and Applications.* Cambridge University Press, 636 pp.

Brown, B. R., M. M. Bell, and A. J. Frambach, 2016: Validation of simulated hurricane drop size distributions using polarimetric radar. *Geophys. Res. Lett.*, **43**, 910–917, doi:10.1002/2015GL067278.

Chan, K. T. F., and J. C. L. Chan, 2016: Sensitivity of the simulation of tropical cyclone size to microphysics schemes. *Adv. Atmos. Sci.*, **33**, 1024–1035, doi:10.1007/s00376-016-5183-2.

Cione, J. G., E. A. Kalina, J. A. Zhang, and E. W. Uhlhorn, 2013: Observations of air–sea interaction and intensity change in hurricanes. *Mon. Wea. Rev.*, **141**, 2368–2382, doi:10.1175/MWR-D-12-00070.1.

Crum, T. D., and R. L. Alberty, 1993: The WSR-88D and the WSR-88D Operational Support Facility. *Bull. Amer. Meteor. Soc.*, **74**, 1669–1687, doi:10.1175/1520-0477(1993)074<1669:TWATWO>2.0.CO;2.

Didlake, A. C., Jr., and R. A. Houze Jr., 2009: Convective-scale downdrafts in the principal rainband of Hurricane Katrina (2005). *Mon. Wea. Rev.*, **137**, 3269–3293, doi:10.1175/2009MWR2827.1.

Fovell, R. G., and H. Su, 2007: Impact of cloud microphysics on hurricane track forecasts. *Geophys. Res. Lett.*, **34**, L24810, doi:10.1029/2007GL031723.

——, K. L. Corbosiero, and H.-C. Kuo, 2009: Cloud microphysics impact on hurricane track as revealed in idealized experiments. *J. Atmos. Sci.*, **66**, 1764–1778, doi:10.1175/2008JAS2874.1.

——, Y. P. Bu, K. L. Corbosiero, W.-W. Tung, Y. Cao, H.-C. Kuo, L.-H. Hsu, and H. Su, 2016: Influence of cloud microphysics and radiation on tropical cyclone structure and motion. *Multiscale Convection-Coupled Systems in the Tropics: A Tribute to Dr. Michio Yanai, Meteor. Monogr.*, No. 56, Amer. Meteor. Soc., doi:10.1175/AMSMONOGRAPHS-D-15-0006.1.

Frame, J., P. Markowski, Y. Richardson, J. Straka, and J. Wurman, 2009: Polarimetric and dual-Doppler radar observations of the Lipscomb County, Texas, supercell thunderstorm on 23 May 2002. *Mon. Wea. Rev.*, **137**, 544–561, doi:10.1175/2008MWR2425.1.

Friedrich, K., E. A. Kalina, J. Aikins, D. Gochis, and R. Rasmussen, 2016a: Precipitation and cloud structures of intense rain during the 2013 Great Colorado Flood. *J. Hydrometeor.*, **17**, 27–52, doi:10.1175/JHM-D-14-0157.1.

——, ——, ——, M. Steiner, D. Gochis, P. A. Kucera, K. Ikeda, and J. Sun, 2016b: Raindrop size distribution and rain characteristics during the 2013 Great Colorado Flood. *J. Hydrometeor.*, **17**, 53–72, doi:10.1175/JHM-D-14-0184.1.

Griffin, E. M., T. J. Schuur, D. R. MacGorman, M. R. Kumjian, and A. O. Fierro, 2014: An electrical and polarimetric analysis of the overland reintensification of Tropical Storm Erin (2007). *Mon. Wea. Rev.*, **142**, 2321–2344, doi:10.1175/MWR-D-13-00360.1.

Herzegh, P. H., and A. R. Jameson, 1992: Observing precipitation through dual-polarization radar measurements. *Bull. Amer. Meteor. Soc.*, **73**, 1365–1374, doi:10.1175/1520-0477(1992)073<1365:OPTDPR>2.0.CO;2.

Heymsfield, A. J., 1972: Ice crystal terminal velocities. *J. Atmos. Sci.*, **29**, 1348–1357, doi:10.1175/1520-0469(1972)029<1348:ICTV>2.0.CO;2.

——, S. Lewis, S. L. Durden, and T. P. Bui, 2006: Ice microphysics observations in Hurricane Humberto: Comparison with non-hurricane generated ice cloud layers. *J. Atmos. Sci.*, **63**, 288–308, doi:10.1175/JAS3603.1.

Hogan, R. J., M. P. Mittermaier, and A. J. Illingworth, 2006: The retrievals of ice water content from radar reflectivity factor and temperature and its use in evaluating a mesoscale model. *J. Appl. Meteor. Climatol.*, **45**, 301–317, doi:10.1175/JAM2340.1.

Houze, R. A., F. D. Marks Jr., and R. A. Black, 1992: Dual-aircraft investigation of the inner core of Hurricane Norbert. Part II: Mesoscale distribution of ice particles. *J. Atmos. Sci.*, **49**, 943–963, doi:10.1175/1520-0469(1992)049<0943:DAIOTI>2.0.CO;2.

Hubbert, J. C., S. M. Ellis, W.-Y. Chang, S. Rutledge, and M. Dixon, 2014a: Modeling and interpretation of S-band ice crystal depolarization signatures from data obtained by simultaneously transmitting horizontally and vertically polarized. *J. Appl. Meteor. Climatol.*, **53**, 1659–1677, doi:10.1175/JAMC-D-13-0158.1.

——, ——, ——, and Y.-C. Liou, 2014b: X-band polarimetric observations of cross coupling in the ice phase of convective

storms in Taiwan. *J. Appl. Meteor. Climatol.*, **53**, 1678–1695, doi:10.1175/JAMC-D-13-0360.1.

Islam, T., P. K. Srivastava, M. A. Rico-Ramirez, Q. Dai, M. Gupta, and S. K. Singh, 2015: Tracking a tropical cyclone through WRF–ARW simulation and sensitivity of model physics. *Nat. Hazards*, **76**, 1473–1495, doi:10.1007/s11069-014-1494-8.

Iwabuchi, H., P. Yang, K. N. Liou, and P. Minnis, 2012: Physical and optical properties of persistent contrails: Climatology and interpretation. *J. Geophys. Res.*, **117**, D06215, doi:10.1029/2011JD017020.

Kalina, E. A., K. Friedrich, S. M. Ellis, and D. W. Burgess, 2014: Comparison of disdrometer and X-band mobile radar observations in convective precipitation. *Mon. Wea. Rev.*, **142**, 2414–2435, doi:10.1175/MWR-D-14-00039.1.

——, ——, B. C. Motta, W. Deierling, G. T. Stano, and N. N. Rydell, 2016: Colorado plowable hailstorms: Synoptic weather, radar, and lightning characteristics. *Wea. Forecasting*, **31**, 663–693, doi:10.1175/WAF-D-15-0037.1.

Kumjian, M. R., 2013: Principles and applications of dual-polarization weather radar. Part III: Artifacts. *J. Oper. Meteor.*, **1**, 265–274, doi:10.15191/nwajom.2013.0121.

——, and A. V. Ryzhkov, 2008: Polarimetric signatures in supercell thunderstorms. *J. Appl. Meteor. Climatol.*, **47**, 1940–1961, doi:10.1175/2007JAMC1874.1.

——, and W. Deierling, 2015: Analysis of thundersnow storms over northern Colorado. *Wea. Forecasting*, **30**, 1469–1490, doi:10.1175/WAF-D-15-0007.1.

Liu, C.-L., and A. J. Illingworth, 2000: Toward more accurate retrievals of ice water content from radar measurement of clouds. *J. Appl. Meteor.*, **39**, 1130–1146, doi:10.1175/1520-0450(2000)039<1130:TMAROI>2.0.CO;2.

Locatelli, J. D., and P. V. Hobbs, 1974: Fall speeds and masses of solid precipitation particles. *J. Geophys. Res.*, **79**, 2185–2197, doi:10.1029/JC079i015p02185.

Lord, S. J., H. E. Willoughby, and J. M. Piotrowicz, 1984: Role of a parameterized ice-phase microphysics in an axisymmetric, nonhydrostatic tropical cyclone model. *J. Atmos. Sci.*, **41**, 2836–2848, doi:10.1175/1520-0469(1984)041<2836:ROAPIP>2.0.CO;2.

Marks, F. D., Jr., and R. A. Houze Jr., 1987: Inner core structure of Hurricane Alicia from airborne Doppler radar observations. *J. Atmos. Sci.*, **44**, 1296–1317, doi:10.1175/1520-0469(1987)044<1296:ICSOHA>2.0.CO;2.

Matrosov, S. Y., 2011: CloudSat measurements of landfalling Hurricanes Gustav and Ike (2008). *J. Geophys. Res.*, **116**, D01203, doi:10.1029/2010JD014506.

——, 2015: The use of CloudSat data to evaluate retrievals of total ice content in precipitating cloud systems from ground-based operational radar measurements. *J. Appl. Meteor. Climatol.*, **54**, 1663–1674, doi:10.1175/JAMC-D-15-0032.1.

——, R. Cifelli, P. J. Neiman, and A. B. White, 2016: Radar rain-rate estimators and their variability due to rainfall type: An assessment based on hydrometeorology testbed data from the southeastern United States. *J. Appl. Meteor. Climatol.*, **55**, 1345–1358, doi:10.1175/JAMC-D-15-0284.1.

May, P. T., J. D. Kepert, and T. D. Keenan, 2008: Polarimetric radar observations of the persistently asymmetric structure of tropical cyclone Ingrid. *Mon. Wea. Rev.*, **136**, 616–630, doi:10.1175/2007MWR2077.1.

McFarquhar, G. M., H. Zhang, G. Heymsfield, R. Hood, J. Dudhia, J. B. Halverson, and F. Marks, 2006: Factors affecting the evolution of Hurricane Erin (2001) and the distributions of

hydrometeors: Role of microphysical processes. *J. Atmos. Sci.*, **63**, 127–150, doi:10.1175/JAS3590.1.

Melnikov, V. M., D. S. Zrnić, R. J. Doviak, P. B. Chilson, D. B. Mechem, and Y. L. Kogan, 2011: Prospects of the WSR-88D radar for cloud studies. *J. Appl. Meteor. Climatol.*, **50**, 859–872, doi:10.1175/2010JAMC2303.1.

——, ——, D. W. Burgess, and E. R. Mansell, 2015: Vertical extent of thunderstorm inflows revealed by polarimetric radar. *J. Atmos. Oceanic Technol.*, **32**, 1860–1865, doi:10.1175/JTECH-D-15-0096.1.

Nousiainen, T., and G. McFarquhar, 2004: Light scattering by quasi-spherical ice crystals. *J. Atmos. Sci.*, **61**, 2229–2248, doi:10.1175/1520-0469(2004)061<2229:LSBQIC>2.0.CO;2.

OFCM, 2016: WSR-88D meteorological observations. Part A: System concepts, responsibilities, and procedures. Federal Meteorological Handbook 11, FCM-H11A-2016, Office of the Federal Coordinator for Meteorological Services and Supporting Research, 21 pp. [Available online at http://www.ofcm.gov/publications/fmh/FMH11/2016FMH11PTA.pdf.]

Palmer, R. D., and Coauthors, 2011: Observations of the 10 May 2010 tornado outbreak using OU-PRIME: Potential for new science with high-resolution polarimetric radar. *Bull. Amer. Meteor. Soc.*, **92**, 871–891, doi:10.1175/2011BAMS3125.1.

Park, H., A. V. Ryzhkov, D. S. Zrnić, and K. Kim, 2009: The hydrometeor classification algorithm for the polarimetric WSR-88D: Description and application to an MCS. *Wea. Forecasting*, **24**, 730–748, doi:10.1175/2008WAF2222205.1.

Protat, A., and C. R. Williams, 2011: The accuracy of radar estimates of ice terminal fall speed from vertically pointing Doppler radar measurements. *J. Appl. Meteor. Climatol.*, **50**, 2120–2138, doi:10.1175/JAMC-D-10-05031.1.

Romine, G. S., D. W. Burgess, and R. B. Wilhelmson, 2008: A dual-polarization-radar-based assessment of the 8 May 2003 Oklahoma City area tornadic supercell. *Mon. Wea. Rev.*, **136**, 2849–2870, doi:10.1175/2008MWR2330.1.

Rosenfeld, D., 1999: TRMM observed first direct evidence of smoke from forest fires inhibiting rainfall. *Geophys. Res. Lett.*, **26**, 3105–3108, doi:10.1029/1999GL006066.

——, W. L. Woodley, A. Khain, W. R. Cotton, G. Carrió, I. Ginis, and J. H. Golden, 2012: Aerosol effects on microstructure and intensity of tropical cyclones. *Bull. Amer. Meteor. Soc.*, **93**, 987–1001, doi:10.1175/BAMS-D-11-00147.1.

Ryzhkov, A. V., 2007: The impact of beam broadening on the quality of radar polarimetric data. *J. Atmos. Oceanic Technol.*, **24**, 729–744, doi:10.1175/JTECH2003.1.

——, D. S. Zrnić, and B. A. Gordon, 1998: Polarimetric method for ice water content determination. *J. Appl. Meteor.*, **37**, 125–134, doi:10.1175/1520-0450(1998)037<0125:PMFIWC>2.0.CO;2.

Snyder, J. C., H. B. Bluestein, G. Zhang, and S. J. Frasier, 2010: Attenuation correction and hydrometeor classification of high-resolution, X-band, dual-polarized mobile radar measurements in severe convective storms. *J. Atmos. Oceanic Technol.*, **27**, 1979–2001, doi:10.1175/2010JTECHA1356.1.

Steiner, M., R. A. Houze, and S. E. Yuter, 1995: Climatological characterization of three-dimensional storm structure from operational radar and rain gauge data. *J. Appl. Meteor.*, **34**, 1978–2007, doi:10.1175/1520-0450(1995)034<1978:CCOTDS>2.0.CO;2.

Tanamachi, R. L., and P. L. Heinselman, 2016: Rapid-scan, polarimetric observations of central Oklahoma severe storms on 31 May 2013. *Wea. Forecasting*, **31**, 19–42, doi:10.1175/WAF-D-15-0111.1.

Van Den Broeke, M. S., 2013: Polarimetric radar observations of biological scatters in Hurricanes Irene (2011) and Sandy (2012). *J. Atmos. Oceanic Technol.*, **30**, 2754–2767, doi:10.1175/JTECH-D-13-00056.1.

Vivekanandan, J., S. M. Ellis, R. Oye, D. S. Zrnić, A. V. Ryzhkov, and J. Straka, 1999: Cloud microphysics retrieval using S-band dual-polarization radar measurements. *Bull. Amer. Meteor. Soc.*, **80**, 381–388, doi:10.1175/1520-0477(1999)080<0381:CMRUSB>2.0.CO;2.

White, A. B., J. R. Jordan, B. E. Martner, F. M. Ralph, and B. W. Bartram, 2000: Extending the dynamic range of an S-band radar for cloud and precipitation studies. *J. Atmos. Oceanic Technol.*, **17**, 1226–1234, doi:10.1175/1520-0426(2000)017<1226:ETDROA>2.0.CO;2.

Wurman, J., D. Dowell, Y. Richardson, P. Markowski, E. Rasmussen, D. Burgess, L. Wicker, and H. Bluestein, 2012: The second Verification of the Origins of Rotation in Tornadoes Experiment: VORTEX2. *Bull. Amer. Meteor. Soc.*, **93**, 1147–1170, doi:10.1175/BAMS-D-11-00010.1.

Yuter, S. E., and R. A. Houze Jr., 1997: Measurements of raindrop size distributions over the Pacific warm pool and implications for *Z–R* relations. *J. Appl. Meteor.*, **36**, 847–867, doi:10.1175/1520-0450(1997)036<0847:MORSDO>2.0.CO;2.

Zrnić, D. S., and A. V. Ryzhkov, 1999: Polarimetry for weather surveillance radars. *Bull. Amer. Meteor. Soc.*, **80**, 389–406, doi:10.1175/1520-0477(1999)080<0389:PFWSR>2.0.CO;2.

——, ——, J. Straka, Y. Liu, and J. Vivekanandan, 2001: Testing a procedure for automatic classification of hydrometeor types. *J. Atmos. Oceanic Technol.*, **18**, 892–913, doi:10.1175/1520-0426(2001)018<0892:TAPFAC>2.0.CO;2.